Cell Reports

Resource

The ULK1 effector BAG2 regulates autophagy initiation by modulating AMBRA1 localization

Graphical abstract

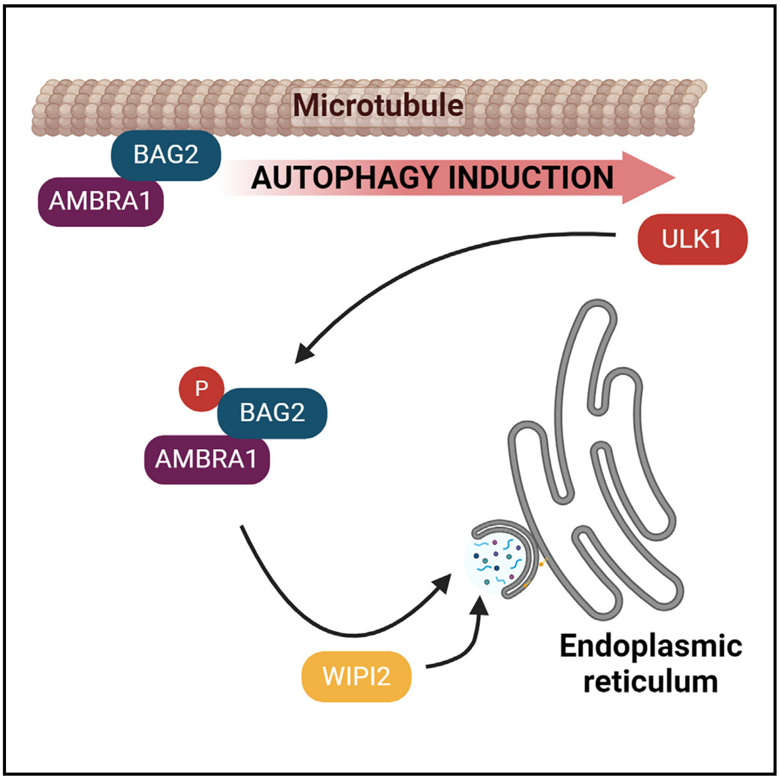

Highlights

- ULK1 complex interacts with protein and lipid kinases and phosphatases forming a signalosome
- In starvation, ULK1 complex members interact with selective autophagy receptors (SARs)
- ULK1 complex interacts and phosphorylates the HSP70 co-chaperone BAG2
- BAG2 has opposing roles in autophagy regulation by modulating ER localization of AMBRA1

Authors

Devanarayanan Siva Sankar, Stephanie Kaeser-Pebernard, Christine Vionnet, ..., Manuela Antonioli, Gian Maria Fimia, Jörn Dengjel

Correspondence

joern.dengjel@unifr.ch

In brief

Sankar et al. generated a deep ULK1-complex interactome using all four complex members as baits. They define the HSP70 co-chaperone BAG2 as bona fide ULK1 target that has opposing roles in autophagy regulation. Unphosphorylated BAG2 sequesters AMBRA1, attenuating autophagy, whereas phosphorylated BAG2 supports ER recruitment of AMBRA1, positively affecting autophagy.

Sankar et al., 2024, Cell Reports *43*, 114689
September 24, 2024 © 2024 The Author(s). Published by Elsevier Inc.
https://doi.org/10.1016/j.celrep.2024.114689

CellPress

Cell Reports

CellPress
OPEN ACCESS

Resource

The ULK1 effector BAG2 regulates autophagy initiation by modulating AMBRA1 localization

Devanarayanan Siva Sankar,[1] Stephanie Kaeser-Pebernard,[1] Christine Vionnet,[1] Sebastian Favre,[1] Lais de Oliveira Marchioro,[3,4] Benjamin Pillet,[1] Jianwen Zhou,[2] Michael Stumpe,[1] Werner Josef Kovacs,[2] Dieter Kressler,[1] Manuela Antonioli,[3,5] Gian Maria Fimia,[3,6] and Jörn Dengjel[1,7,*]
[1] Department of Biology, University of Fribourg, 1700 Fribourg, Switzerland
[2] Institute of Molecular Health Sciences, ETH Zürich, 8093 Zürich, Switzerland
[3] Department of Epidemiology, Preclinical Research and Advanced Diagnostics, National Institute for Infectious Diseases IRCCS "L. Spallanzani", 00149 Rome, Italy
[4] Department of Pharmacology, Federal University of São Paulo (UNIFESP), São Paulo CEP 05508-000, Brazil
[5] Department of Biology, University of Rome "Tor Vergata", 00133 Rome, Italy
[6] Department of Molecular Medicine, University of Rome "Sapienza", 00185 Rome, Italy
[7] Lead contact
*Correspondence: joern.dengjel@unifr.ch
https://doi.org/10.1016/j.celrep.2024.114689

SUMMARY

Autophagy initiation is regulated by the ULK1 kinase complex. To gain insights into functions of the holo-complex, we generated a deep interactome by combining affinity purification- and proximity labeling-mass spectrometry of all four complex members: ULK1, ATG13, ATG101, and RB1CC1/FIP200. Under starvation conditions, the ULK1 complex interacts with several protein and lipid kinases and phosphatases, implying the formation of a signalosome. Interestingly, several selective autophagy receptors also interact with ULK1, indicating the activation of selective autophagy pathways by nutrient starvation. One effector of the ULK1 complex is the HSC/HSP70 co-chaperone BAG2, which regulates the subcellular localization of the VPS34 lipid kinase complex member AMBRA1. Depending on the nutritional status, BAG2 has opposing roles. In growth conditions, the unphosphorylated form of BAG2 sequesters AMBRA1, attenuating autophagy induction. In starvation conditions, ULK1 phosphorylates BAG2 on Ser31, which supports the recruitment of AMBRA1 to the ER membrane, positively affecting autophagy.

INTRODUCTION

Macroautophagy (hereafter referred to as autophagy) is an evolutionarily conserved lysosomal degradation pathway critical for cellular homeostasis.[1] Autophagy is a constitutive process as well as a stress response that mainly fulfills cytoprotective functions. Its dysregulation is often observed in diseases such as cancer and neurodegeneration.[2] A hallmark of autophagy is the *de novo* formation of double membrane vesicles, autophagosomes, which enwrap cytoplasm destined for degradation. Autophagosome biogenesis can be classified by five phases: initiation, membrane nucleation, expansion, pore closure/maturation, and fusion with lysosomes.[3] Each phase is characterized by the involvement of specific genes and respective proteins, which are regulated on transcriptional, translational, and post-translational levels.[4,5] Immediately after a given stress stimulus, autophagosome initiation does not require *de novo* protein synthesis and is mainly regulated on a post-translational level by a set of protein and lipid kinases.[6] The serine/threonine kinase unc-51-like autophagy activating kinase 1 (ULK1, or its homolog ULK2), the mammalian homolog of yeast autophagy-regulated (Atg) 1,[7,8] is the most proximal protein kinase specifically regulating canonical autophagosome biogenesis. The catalytic subunit ULK1, along with ATG13[9,10] and ATG101,[11,12] forms an asymmetric complex with RB1CC1/FIP200,[13] with 1:1:1:2 stoichiometry.[14] Upon autophagy induction, this complex is recruited to ER subdomains,[15] where it phosphorylates several proteins important for functional autophagy, among others the members of the lipid kinase VPS34 complex I.[16,17]

In the current study, we employed state-of-the-art mass spectrometry (MS)-based proteomics to revisit ULK1 complex protein-protein interactions. In contrast to the majority of published approaches that used classical affinity purification (AP)-MS,[18,19] we used a combination of AP- and proximity labeling (PL)-MS to generate a deep interactome of the ULK1 holo-complex. PL-MS relies on the expression of proteins of interest (POIs) fused to enzymes covalently transferring chemical groups to proximal proteins labeling so-called protein neighborhoods (for review, see Siva Sankar and Dengjel[20]). Using this double strategy, we generated a comprehensive picture of ULK1 complex interactions, characterizing common and subunit-specific interaction partners.

One protein that caught our attention and was studied in detail is Bcl-2-associated athanogene 2 (BAG2), which interacts via its

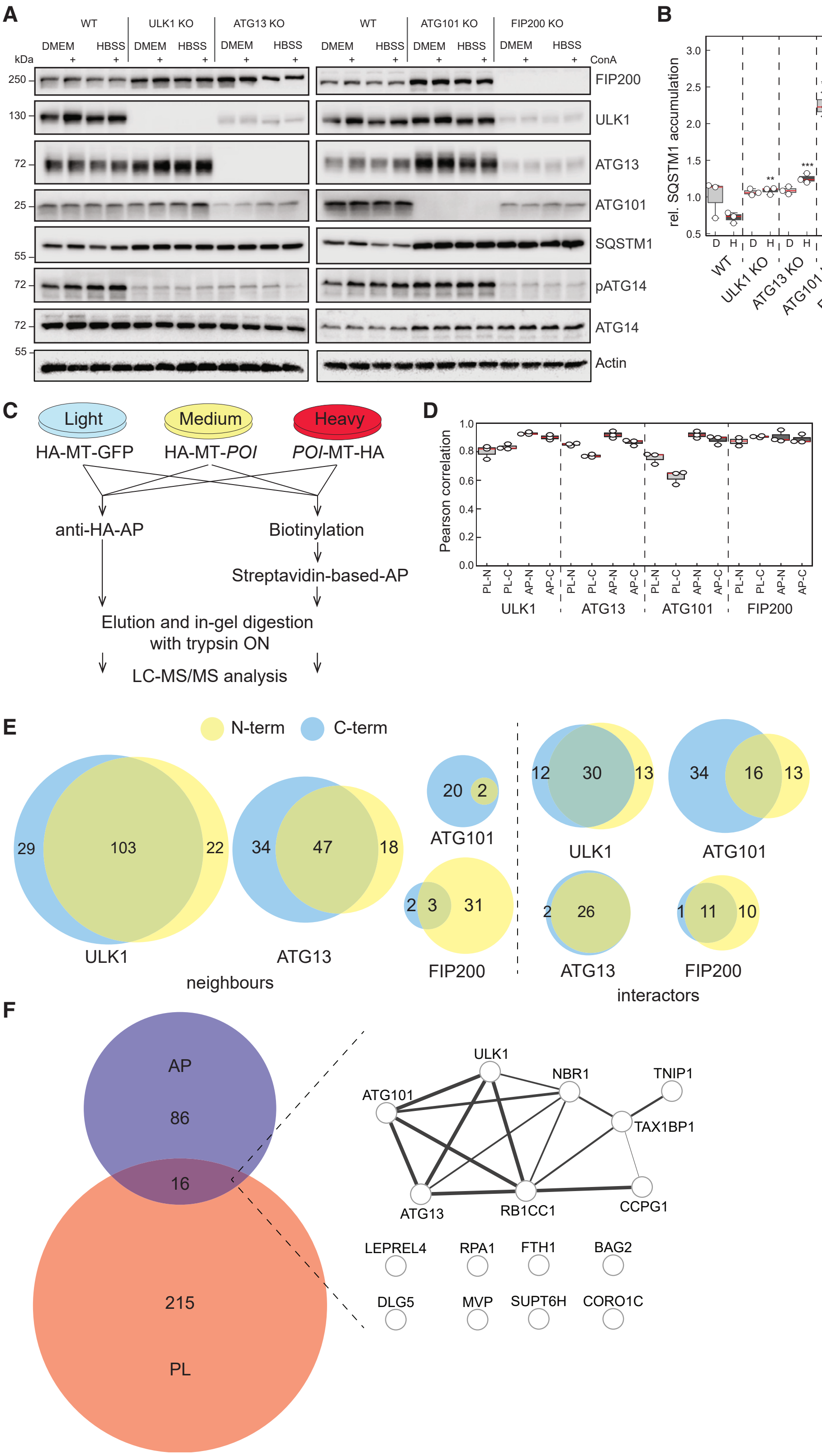

(legend on next page)

BAG domain with HSC/HSP70 proteins, acting as a nucleotide exchange factor.[21] BAG2 is a member of the evolutionarily conserved BAG family, which in humans consists of six members, BAG1–BAG6. BAG proteins are suggested to act antiapoptotically and were shown to modulate proteasomal as well as autophagosomal protein degradation.[22,23] BAG2 is widely expressed[24] and localizes to various subcellular locations such as mitochondria,[25] ER,[26] and microtubules.[27] It seems to modulate the balance between chaperone-mediated protein folding and chaperone-mediated protein degradation, among others by inhibiting CHIP, an HSC/HSP70 chaperone-associated ubiquitin ligase.[26] Similarly to BAG3 and BAG6, BAG2 was shown to promote mitophagy[25,28–30] and reticulophagy via its interaction with the selective autophagy receptor (SAR) SQSTM1/p62 in the context of *Mycobacterium tuberculosis* infection.[31]

Here, we characterize BAG2 as ULK1-complex interactor, target, and downstream effector, one of its autophagy-relevant clients being the VPS34- and E3-ubiquitin ligase complex member, activating molecule in BECN1-regulated autophagy protein 1 (AMBRA1).[32] Under growth conditions BAG2 sequesters AMBRA1, attenuating autophagy; however, upon autophagy activation, BAG2 translocates to ER subdomains supporting AMBRA1-ER localization and functional autophagy. Changes in the intracellular localization of BAG2 are regulated by ULK1 via phosphorylation of BAG2 at Ser31.

RESULTS

The ULK1 holo-complex interacts with selective autophagy receptors in starvation conditions

Protein-protein interactions of ULK1 complex members have been analyzed by AP-MS and PL-MS in low- and high-throughput studies[18,33,34] (for review, see Siva Sankar and Dengjel[20]). Depending on the experimental setup (e.g., AP of endogenous or tagged proteins, tag localization), different sets of interaction partners might be identified. To generate a comprehensive overview of ULK1 complex interactions, we generated a deep ULK1 complex interactome under nutrient starvation by combining AP- and PL-MS of N- and C-terminal-tagged fusion proteins. First, using CRISPR-Cas9 we generated four HeLa knockout (KO) cell lines, one for each complex member, i.e., ULK1, ATG13, ATG101, and FIP200, respectively (Figure 1A). As anticipated, all four cell lines exhibit a block in autophagy as analyzed by accumulation of p62/SQSTM1 under starvation conditions (Figure 1B). Interestingly, loss of single complex members has differential effects on abundances of the other members (Figure 1A): loss of FIP200 leads to a downregulation of all the other complex members, supporting its central function in complex assembly.[14] In contrast, loss of ATG101 and ULK1 lead to compensatory effects and increased abundances of the other members. Loss of ATG13 has a positive effect on the abundance of FIP200 and negative effects on ULK1 and ATG101.[12,35] These data imply that the holo-complex forms by preassembled subcomplexes.[14] Loss of complex members also differentially affects ULK1 activity as analyzed by phosphosite-specific western blots against the ULK1 target site on ATG14, Ser29 (Figure 1A, pATG14). Whereas KO of ULK1, ATG13, and FIP200 leads to reduced ATG14 phosphorylation, KO of ATG101 does not. This implies that loss of ATG101 does not interfere with ULK1 complex assembly and activity per se but, rather, negatively interferes with the recruitment of downstream components such as ATG9,[36] which ultimately also leads to a block of functional autophagy (Figure 1B).

In each KO cell line, we introduced an inducible expression system supporting the doxycycline (dox)-controlled expression of either the respective N-terminal- or C-terminal-tagged protein of interest (POI) (Figure S1). As tag we used a combination of the peptide epitope of human influenza virus hemagglutinin (HA) and the biotin ligase variant miniTurbo (MT),[37] supporting both AP- and PL-MS analyses (Figure 1C).[38] Using stable isotope labeling by amino acids in cell culture (SILAC)-based proteomics, we determined the interactions of ULK1 complex members under starvation conditions (90 min of Hanks' balanced salt solution [HBSS] treatment), the classical stimulus inducing bulk autophagy, by comparing POI- to HA-MT-GFP-based enrichments as negative controls (Figure 1C). For each analysis, i.e., AP- and PL-MS of N- and C-terminal-tagged POI, we performed three biological replicates, which led to a total of 48 liquid chromatography-tandem mass spectrometry (LC-MS/MS) experiments, 24 AP-MS and 24 PL-MS studies (Tables S1A and S1B). Biological replicates correlate well with an average Pearson correlation coefficient of 0.85 (Figure 1D, range 0.57–0.93). Interestingly, the PL-MS studies of ATG101 show reproducibly the lowest correlation (Figure 1D, range 0.57–0.78). ATG101 is with 25 kDa by far the smallest protein of the complex, and the low correlation of transient interactions identified by PL-MS might indicate high mobility of ATG101. High-confidence interactors are defined as proteins that are identified as significantly enriched compared to HA-MT-GFP in minimally two AP-MS or two PL-MS experiments, respectively (significance A, $p < 0.05$, Benjamini-Hochberg [BH]-corrected for PL-MS, see STAR Methods for details). As expected, PL-MS yields more

Figure 1. Deep interactome of the ULK1 holo-complex

(A) HeLa KO cell lines of ULK1 complex members were generated by CRISPR-Cas9 using specific single-guide RNAs. Shown is one representative western blot of $n = 3$ biological replicates. ConA, concanamycin A; pATG14, phosphorylated Ser29 of ATG14; WT, wild type. Cells were starved in HBSS for 90 min.

(B) Blocked autophagy in KO cell lines. Quantification of blots shown in (A) normalized to actin. All KO cells exhibit an accumulation of SQSTM1/p62 in starvation conditions. D, DMEM; H, HBSS. $n = 3$ biological replicates, Student's t test, unpaired; $^{**}p < 0.01$, $^{***}p < 0.001$. Boxplots show spreads of relative protein abundances. Single values are highlighted as white dots.

(C) Quantitative proteomics workflow. KO cells were stably transfected with doxycycline (dox)-inducible expression constructs encoding N- or C-terminal-tagged proteins of interest (POI). Affinity purifications (AP) and proximity labeling (PL) were performed prior to quantitative LC-MS/MS analyses.

(D) Correlation of biological replicates. For each POI and each tag-variant, $n = 3$ biological replicates were performed.

(E) Proportional Venn diagrams highlighting overlap of significantly enriched neighbors and interactors ($p < 0.05$, see STAR Methods for details).

(F) Proportional Venn diagram highlighting overlap of significantly enriched interactors identified by AP-MS and PL-MS. The 16 commonly identified proteins were analyzed by STRING DB for known protein-protein interactions. Edge thickness indicates confidence of interactions.

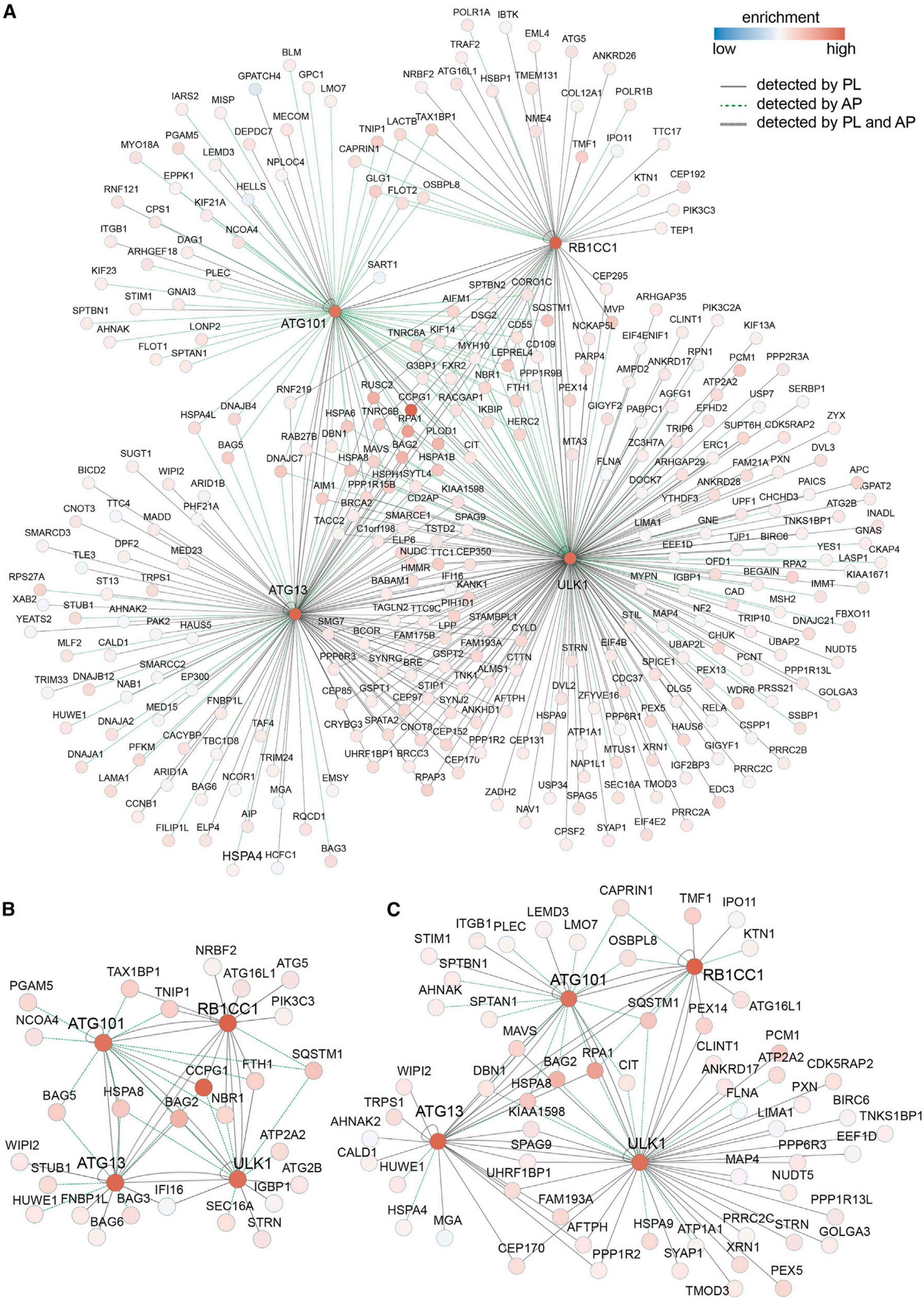

(legend on next page)

significantly enriched proteins compared to AP-MS, one exception being ATG101 (Figure 1E). The localization of the tag does have an influence on the identified interactions in both approaches. The most prominent differences are observed for the PL-MS analyses of ATG101 and FIP200 (Figure 1E). Whereas the N-terminal-tagged version of FIP200 reveals 34 neighboring proteins, only five are enriched with the C-terminal variant. This reduced efficiency might be linked to the structure of the ULK1 holo-complex, in which two FIP200 protomers form a homodimer via their C-terminal regions and claw domains.[14,39] The C-terminal tag might interfere with holo-complex formation. For ATG101 the C-terminal tagged variant yields a higher number of potential neighbors, which might highlight better accessibility compared to the N-terminal variant.[40] The N-terminal region of ATG101 has been shown to be important for functional autophagy, potentially affecting complex assembly by being involved in the dimerization with ATG13.[36]

In total we identified 317 proteins as neighbors and interactors (Figure 1F; Tables S1C and S1D). Compared to other published ULK1 complex interactomes, we cover 65 known and 252 non-characterized interactors (Figure S2A).[18,33,34] As has been described for AP- and PL-MS studies,[38,41] both approaches are complementary and uncover different sets of interacting and neighboring proteins. Using our stringent selection criteria, only 16 proteins, i.e., ca. 5% of the entire dataset, are identified by both approaches, among them the four holo-complex members themselves (Figure 1F). Intriguingly, the SARs CCPG1, NBR1, and TAX1BP1 appear to interact closely with the ULK1 complex as they are among the 16 commonly enriched proteins.[42–44] In selective autophagy, the recruitment of the ULK1 complex to degradation-primed cargo via interaction between FIP200 and SARs has been recognized as a decisive event,[39,45–47] TAX1BP1 being the main driver by FIP200 binding.[48] Our finding indicates that also under starvation-induced autophagy, i.e., the prototypical stimulus of non-selective bulk autophagy, selective removal of cargo takes place. Indeed, of the remaining proteins, TNIP1,[49,50] MVP,[51] FTH1,[52] and P3H4[53] have been identified as selective autophagosomal cargo (Figure 1F). Interestingly the HSC/HSP70 co-chaperone BAG2 has been linked to the regulation of reticulophagy,[31] which is why we studied it in more detail (see further below).

The ULK1 complex forms a signaling hub

The best-known function of the ULK1 complex is the induction of autophagy. Other functions are less well understood; however, analyses of its molecular targets indicate that it also regulates later stages of autophagy, such as autophagosome-lysosome fusion,[54,55] and that it may affect other pathways, ranging from glycolysis[56] to mRNA splicing.[57] Our deep interactome reveals that out of the 317 interactors, 102 interact with minimally two complex members and 215 are member-specific interactors (Figure 2A). As a quality check, we scanned the interactome for proteins with known functions in autophagy and were able to generate a subnetwork of 31 proteins, i.e., ca. 10% of the entire dataset (Figure 2B). These proteins are mainly linked to early events in autophagy, such as membrane nucleation (PIK3C3, ATG16L1) and expansion (ATG2B, ATG5, WIPI2), as well as to cargo recruitment. Next to the SARs mentioned above, we identified p62/SQSTM1,[58] interestingly only by AP-MS and not by PL-MS, as well as NCOA4 and FTH1, which regulate ferritin degradation and iron homeostasis.[52]

The identified 317 proteins are linked to numerous subcellular localizations as well as many functions, indicating a much broader role of ULK1 in shaping the cellular response to starvation. The wealth of interactions indicates that the ULK1 complex acts as a signaling hub, i.e., it forms a macromolecular signalosome. We identified the ULK1 complex as interacting with five protein kinases, two lipid kinases, and two metabolite kinases (Figure S2B), as well as with 11 regulatory phosphatase subunits (Figure S2C). Finally, we scanned the entire interactome for known and potential ULK1 targets and generated a subnetwork consisting of the four complex members and 60 published target proteins (Figure 2C).[17,19,54,56,59,60] The network contains proteins related to autophagy (false discovery rate [FDR] = 0.0129), such as p62/SQSTM1, ATG16L1, and WIPI2, but also many proteins related to cytoskeleton (FDR = 0.00031) and intracellular transport (FDR = 0.0071), indicating that ULK1 also regulates autophagosome trafficking. Taken together, we generated a comprehensive list of proteins interacting or being in close spatial proximity with the ULK1 holo-complex under starvation conditions. Many of these are ULK1 targets and are related to autophagy regulation or signal transduction, supporting the interpretation that ULK1 complexes form macromolecular signalosomes.

The co-chaperone BAG2 is a ULK1 interactor that modulates functional autophagy

The HSC/HSP70 co-chaperone BAG2 caught our attention,[61] as it was one of the 16 proteins that were identified by both AP- and PL-MS approaches (Figure 1F) and as it carries a potential ULK1 phosphorylation site (Figure 2C). We identified BAG2 as a significant interaction partner of ULK1, ATG101, and ATG13 by MS analyses (Figure 2A) as well as by biotin-based AP-western blot (Figure S1). To test whether these interactions are potentially direct, we expressed BAG2 and the three ULK1-complex members in yeast and performed two-hybrid assays. Only in the case of the C-terminal domain of ULK1 (amino acids 827–1,050, abbreviated as ULK1.827C) did we observe activation of the *HIS3* and *ADE2* reporter genes and, thus, growth on selective medium lacking histidine or adenine, indicating that the ULK1-BAG2 interaction is likely direct. The interactions of BAG2 with ATG13 and ATG101 might be indirect, as we did not observe activation of the reporter genes (Figure S3). In ULK1 AP-MS experiments, BAG2 is enriched to a similar extent as the other

Figure 2. The ULK1 holo-complex forms a signaling hub

(A) Deep ULK1 complex interactome. Shown are significant protein-protein interactions identified by AP-MS and PL-MS under starvation conditions (90 min of HBSS treatment). Node color indicates relative enrichment in all 48 experiments highlighted in Figure 1D. Edge color indicates the type of performed experiments.

(B) ULK1 complex interactors with known functions in autophagy.

(C) ULK1 complex interactors that were identified as potential ULK1 targets.

complex members (Figure 3A). To confirm these findings, we tested the interactions in a reverse co-AP of ectopically expressed tagged BAG2 followed by western blot analysis against ULK1 and ATG13 (Figures 3B and 3C, $n = 3$). Starvation appears to stabilize the interaction of BAG2 and ULK1; however, the difference is not statistically significant. As the BAG2-ATG13 interaction is similar in growth and starvation conditions, we conclude that BAG2 is likely a constitutive interaction partner of the ULK1 complex.

We next asked whether BAG2 supports functional autophagy. For this we generated (1) CRISPR-Cas9-based HeLa KO cells using single-guide RNAs (see STAR Methods) and (2) HeLa knockdown (KD) cells using a short hairpin (shRNA)-based approach. With respect to KO cells, we generated two cell clones that were negative for BAG2 using limiting dilution. We first analyzed autophagy flux in KO cells monitoring MAP1LC3A/B (LC3) and GABARAP lipidation levels in the absence and presence of bafilomycin A1 (BafA1), which blocks lysosomal acidification and thus inhibits lysosomal protein degradation (Figures 3D–3F). Both clones exhibit an accumulation of lipidated LC3 and GABARAP in the absence of BafA1, especially under starvation conditions (Figures 3D and 3E). As the maximal lipidation level under BafA1 treatment does not increase in *BAG2* KO clones compared to wild-type (WT) cells, this leads to a reduction in autophagosome turnover, i.e., autophagy flux (Figure 3F). Also by MS, we identified an accumulation of LC3 and p62 in KO cells, which leads to decreased protein flux under starvation conditions (Figures S4A and S4B). In agreement, p62 puncta accumulate in KO cells as analyzed by immunofluorescence (IF) (Figures S4C and S4D).

Interestingly and in stark contrast to KO cells, KD cells do not present an accumulation of lipidated LC3 and GABARAP in the absence of BafA1 (Figures 3G and 3H), *BAG2* KD consequently leading to an increase in autophagy flux (Figure 3I). This is also seen by employing the Halo-Tag reporter system[62] (Figures S4E and S4F), as well as by p62 puncta analysis by IF (Figures S4G and S4H). Thus, whereas chronic removal of BAG2 leads to a reduction, acute removal leads to an increase in autophagy flux.

To address this discrepancy, we monitored autophagosome-lysosome fusion by analyzing p62-LAMP2 co-localization by IF. Whereas we observed an increase in p62-LAMP2 co-localization in WT cells when lysosomal acidification was blocked by BafA1 and when autophagy was induced by starvation, we failed to observe this in *BAG2* KO cells, indicating that lysosomal targeting of autophagosomes is perturbed by the chronic loss of BAG2 (Figures 4A and 4C). Importantly, re-expression of *BAG2* in KO cells rescues this phenotype, highlighting that the observed perturbation is indeed BAG2 dependent (Figure S5). In contrast, in shRNA-mediated BAG2 KD cells, p62-LAMP2 co-localization behaves similarly to control cells using a scrambled shRNA, indicating that lysosomal targeting of autophagosomes is not perturbed by the acute loss of BAG2 (Figures 4B and 4D). Taken together, the acute effect of loss of BAG2 is an increase in autophagy flux. Under prolonged absence in KO cells, loss of BAG2 appears to have secondary effects that interfere with vesicle trafficking, leading to a reduction in autophagosome-lysosome fusion, which results in a net reduction of autophagy activity.

BAG2 changes interactions and intracellular localization in response to autophagy induction

Having established that BAG2 modulates autophagy, we next aimed to elaborate potential underlying mechanisms. For this, we expressed N-terminally HA-streptactin (SHA)-tagged BAG2 in *BAG2* KO cells by lentiviral infection and analyzed BAG2 interaction partners by AP-MS in both growth and starvation conditions. In three biological replicates each, we identified 736 proteins as significantly enriched when comparing SHA-BAG2-APs to respective negative controls, i.e., dox-treated BAG2 KO cells infected with a lentiviral control vector (total of 12 APs, $q < 0.05$, Tables S3A–S3C). Of these, 97 bind more strongly in starvation and 27 more strongly in growth conditions (Figure 5A, $q < 0.05$; Table S3C). Analyzing enriched gene ontology (GO) terms to identify stimulus-dependent alterations, it appears that BAG2 changes its subcellular localization upon starvation. Whereas we identified several tubulin subunits as enriched under growth conditions, indicating a microtubular localization (Figures 5A and 5B), in autophagy-inducing conditions enriched proteins carry GO terms related to endomembranes, such as the COPII coat protein SEC13 and the ER exit sites (ERES) marker SEC16A, one principal site of autophagosome biogenesis (Figures 5A and 5B).[63,64] Focusing on starvation-specific proteins that carry the GO term "endomembrane system," we were able to generate a protein interaction network of 46 proteins using STRING DB (Figure 5C).[65] One of the most strongly binding proteins in starvation conditions is the ER/Golgi-localized chloride ion channel CLCC1, mutations of which have been associated with retinitis pigmentosa (Figures 5A and 5C).[66] To further characterize the CLCC1-positive membrane compartment in our experimental setup, its co-localization with membrane-bound organelle markers was analyzed by IF. We observed partial co-localization of CLCC1 with LMAN1/ERGIC-53 and SEC13, but not with SNX1, indicating that CLCC1 localizes at least partially to the ER-Golgi intermediate compartment in HeLa cells (Figure S6A).

To test whether observed changes in protein interactions reflect a change in subcellular localization, we performed a crude cell fractionation separating microvesicles, i.e., the 17,000 × *g* fraction containing ER, Golgi, endosomes, and lysosomes[67] from cytosol, nuclei, and mitochondria and observed an increased abundance of BAG2 in the RAB7-positive cell fraction in starvation (Figures 5D and 5E). Also by IF, we observed that BAG2 co-localizes significantly more strongly with CLCC1 in starvation conditions (Figures 5F and 5G). It appears that BAG2 localizes to numerous membrane-bound compartments in starvation, as the co-localization with the ERES marker SEC16A, the Golgi marker TGN46, the endosome marker VPS35, and the lysosome marker LAMP2 also increases (Figures S7), corroborating interaction data (Figures 5A–5C). Importantly, BAG2 localization and its interaction with CLCC1 are dependent on ULK1 activity. The ULK1 inhibitor MRT68921 reduces the BAG2-CLCC1 interaction as analyzed by AP coupled to western blot (Figures 5H and 5I)[68] and by IF-based co-localization (Figures S6B and S6C). Also in ULK1 KO cells, BAG2 responds less to starvation, and the co-localization with CLCC1 is significantly reduced (Figures S6D and S6E). Taken together, under starvation, i.e., autophagy induction, a pool of

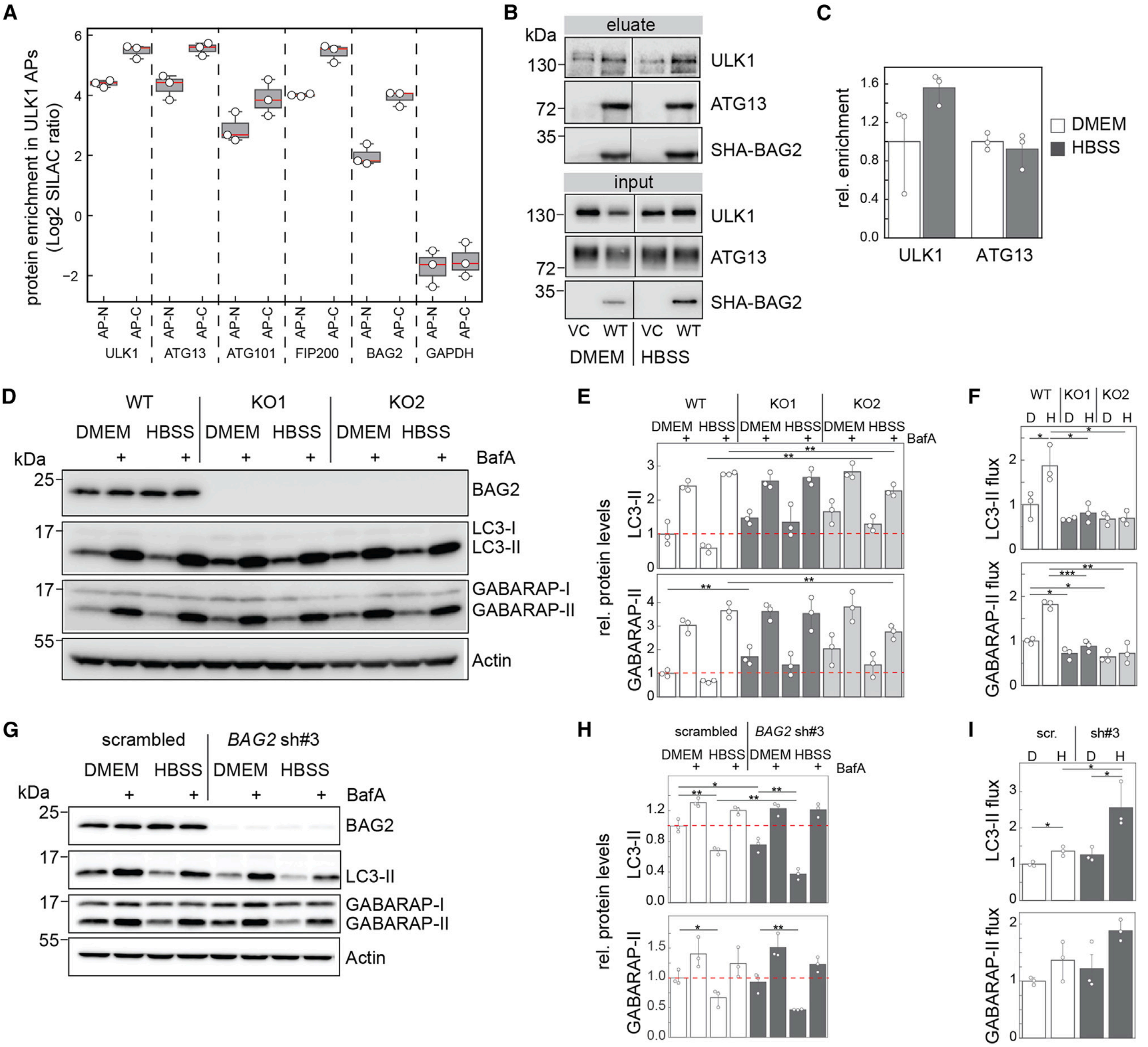

Figure 3. BAG2 is a constitutive interaction partner of ULK1 modulating autophagy

(A) BAG2 binds to ULK1 similarly to its complex members in AP-MS. Shown are normalized and $\log_2$-transformed SILAC ratios using N- and C-terminal-tagged ULK1 variants. GAPDH is depicted as negative control ($n = 3$ biological replicates each). Boxplots show spreads of ratios. Single values are highlighted as white dots.

(B and C) (B) Co-immunoprecipitation (coIP) of SHA-tagged BAG2 and its interaction partners ULK1 and ATG13. Shown is one representative experiment of $n = 3$ biological replicates. Equal protein amounts per lane were loaded. Samples were run on one gel, and black lines indicate cropping of unrelated lanes; these data were also used to generate Figures 6B and 7D. (C) Quantification of $n = 3$ replicates.

(D–F) *BAG2* KO reduces autophagy flux. Shown is one representative blot of $n = 3$ biological replicates (D). Actin serves as loading control. Cells were starved in HBSS and/or treated with BafA1 for 3 h. Respective quantification of LC3-II and GABARAP-II bands relative to actin are shown in (E). Red dotted lines indicate protein levels in DMEM control conditions. Comparing BafA1-treated with non-treated lanes indicates reduced autophagy flux in KO compared to WT cells (F).

(G–I) *BAG2* KD increases autophagy flux. Shown is one representative blot of $n = 3$ biological replicates (G). Actin serves as loading control. Cells were starved in HBSS and/or treated with BafA1 for 3 h. Respective quantification of LC3-II and GABARAP-II bands are shown in (H). Red dotted lines indicate protein levels in DMEM control conditions. Comparing BafA1-treated with non-treated lanes indicates increased autophagy flux in KD compared to control cells (I).

Student's t test, unpaired; *$p < 0.05$, **$p < 0.01$, ***$p < 0.001$. Single values are highlighted as white dots. Error bars indicate 95% confidence interval.

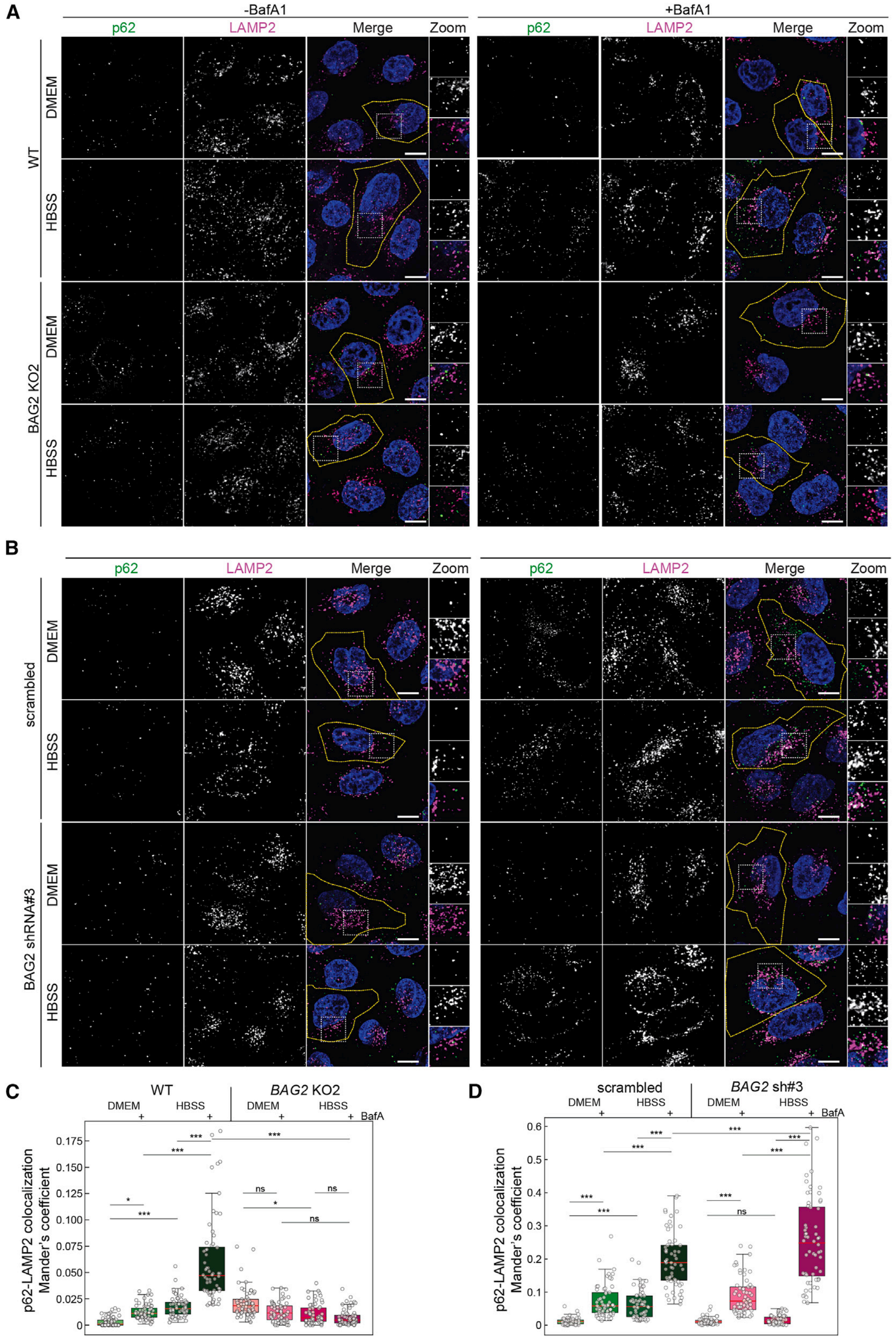

(legend on next page)

BAG2 changes its subcellular localization and protein-protein interactions in a ULK1-dependent manner, localizing to CLCC1-positive endomembranes, which include membranes that are positive for SEC13 and SEC16A being indicative for ERES, sites at which autophagosome biogenesis takes place.

In nutrient starvation, BAG2 supports AMBRA1 recruitment to the ER

One of the proteins that we found reproducibly significantly enriched in starvation conditions by MS-based proteomics of exogenous and endogenous BAG2 APs and that has a known function in autophagy regulation is the VPS34 complex member AMBRA1 (Figures 5A and 6A).[32,69] In agreement, we also identified an increased interaction between AMBRA1 and BAG2 in starvation conditions by comparing APs of tagged BAG2 using western blot (Figures 6B and 6C) as well as by immunoprecipitations (IPs) of endogenous AMBRA1 using MS as readout (Figure 6D). Thus, AMBRA1 binds to BAG2, and this binding is increased by limited nutrient availability. The interaction of AMBRA1 with BAG2 might be direct or indirect via HSC/HSP70 members. To discriminate these two options, we expressed the HSC70-binding-deficient BAG2 variant, $BAG2^{I160A}$,[70] in *BAG2* KO cells and compared its interactome to $BAG2^{WT}$ cells by AP-MS. As anticipated, HSPA4 and HSPA9 bind more weakly to $BAG2^{I160A}$ (Figure 6E), as does CLCC1, indicating that the latter might interact indirectly with BAG2 via HSC70 proteins. Interestingly, AMBRA1 binds equally well to both BAG2 variants, implying that this interaction is potentially direct and independent of HSC/HSP70-BAG2 interactions (Figure 6E). In agreement with this observation, we did not identify AMBRA1 in endogenous CLCC1 IPs and, vice versa, CLCC1 in endogenous AMBRA1 IPs (Figures 6D and S8A). To address the relevance of the BAG2-AMBRA1 interaction, we studied the subcellular localization of AMBRA1 in HeLa WT and *BAG2* KO clones by IF. In the absence of BAG2, we observed a perturbed intracellular distribution of AMBRA1. Whereas one could observe an increased localization of AMBRA1 to the ER membrane in starvation in WT cells, KO cells, especially KO1, lost their ability to respond to starvation and exhibited an increased localization of AMBRA1 to the ER membrane also in growth conditions (Figures 6F and 6G). This implies that one role of BAG2 in autophagy is the regulation of the subcellular distribution of AMBRA1, sequestering AMBRA1 in growth conditions, potentially at microtubuli (Figure S8B),[71] and interfering with its localization to the ER membrane. To analyze whether the observed changes in AMBRA1 localization mirror changes in VPS34-complex activity affecting the local production of phosphatidylinositol 3-phosphate (PI3P), we monitored WIPI2 puncta formation in WT and *BAG2* KO cells. WIPI2, an ortholog of yeast Atg18, is a PI3P-binding protein important for autophagosome expansion.[72] Its local accumulation in puncta can be used as a proxy to address VPS34 activity.[73,74] Reflecting the observation in ER-AMBRA1 localization, we also identified an increase in WIPI2 puncta in BAG2 KO cells in growth conditions that does not further increase under starvation conditions, in contrast to WT cells (Figures 6H and 6I). This increase is dependent on the absence of BAG2, as its ectopic re-expression in KO cells rescues this phenotype (Figures 6H and 6I). We observed the same phenotype in cells acutely depleted of BAG2 by shRNA (Figures S8C and S8D). Thus, our results imply that acute or chronic loss of BAG2 leads to an increase in WIPI2-positive autophagosome nucleation sites.

BAG2 Ser31 is a ULK1 target site regulating its protein interactions and subcellular localization

We addressed the question of whether ULK1 may directly regulate localization and/or protein-protein interactions of BAG2 by phosphorylation. In a phosphoproteomic screen, we identified Ser31 of BAG2 as a potential ULK1 target site.[54] Ser31 lies within a predicted coiled-coil region and is highly conserved in mammals, and the surrounding amino acids fit to the ULK1 consensus motif with a leucine in the -3 position (Figure 7A).[59] To test whether ULK1 indeed directly phosphorylates BAG2 at amino acid residue Ser31, we performed filter-aided *in vitro* kinase assays coupled to MS-based quantification of phosphopeptides.[75] In brief, BAG2 purified from HeLa cells was dephosphorylated by λ-phosphatase and incubated with purified $ULK1^{WT}$ or a kinase-dead variant of ULK1 ($ULK1^{KD}$), in which Asp165 is replaced by Ala,[76] and phosphopeptides were enriched and quantified by LC-MS/MS using extracted ion currents. Whereas we identified the tryptic peptide carrying the Ser31 phosphorylation site in six biological replicates using $ULK1^{WT}$ as kinase, we identified it only once and in less abundance in *in vitro* kinase assays using $ULK1^{KD}$ (Figure 7B). Non-phosphorylated peptides of BAG2 were present in similar amounts. Thus, Ser31 of BAG2 fulfills all requirements of being a bona fide ULK1 target site.

To address the functional relevance of the identified phosphosite, we generated a non-phosphorylatable Ala variant ($BAG2^{S31A}$, S31A) and a phosphomimicking Glu variant ($BAG2^{S31E}$, S31E) of BAG2 and expressed them in *BAG2* KO cells. By both AP-MS and AP-western blot, we observed increased interaction of CLCC1 with $BAG2^{S31E}$ under starvation conditions (Figures 7C–7E; Table S4), albeit only the latter analysis exhibited significant changes. In contrast, the interactions of BAG2 with AMBRA1 and ATG13 are not affected by the site variants, whereas the interaction with p62 is significantly decreased (Figures 7D and 7E). In agreement with the presented biochemical data, IF analyses of cells expressing the various BAG2

Figure 4. Perturbed autophagosomal-lysosomal targeting upon chronic loss of BAG2

(A and B) Fluorescent micrographs labeled with indicated primary antibodies of BAG2 WT and KO cells (A), as well as HeLa cells transduced with *BAG2* or scrambled shRNA-expressing lentiviruses serving as control (B). Untreated (DMEM) or starved (HBSS, 3 h) conditions supplemented or not with 2 nM BafA1 are analyzed. One representative image out of $n = 3$ biological replicates is shown. Scale bars, 10 μm.

(C and D) Co-localization of p62/SQSTM1 and LAMP2 analyzed by immunofluorescence (IF) in (A) and (B). Shown is the proportion of the LAMP2 signal that coincides with the p62/SQSTM1 signal using thresholded Mander's B coefficient. In WT and KD cells, co-localization increases upon starvation and upon BafA1 treatment. This is not the case in KO cells. $n = 3$ biological replicates each, 20 cells per replicate. White dots represent the co-localization foci count per cell and replicate. A two-way ANOVA test followed by Tukey's HSD post hoc test was used to identify significant differences. ns, not significant; $^{*}p \leq 0.05$, $^{***}p \leq 0.001$.

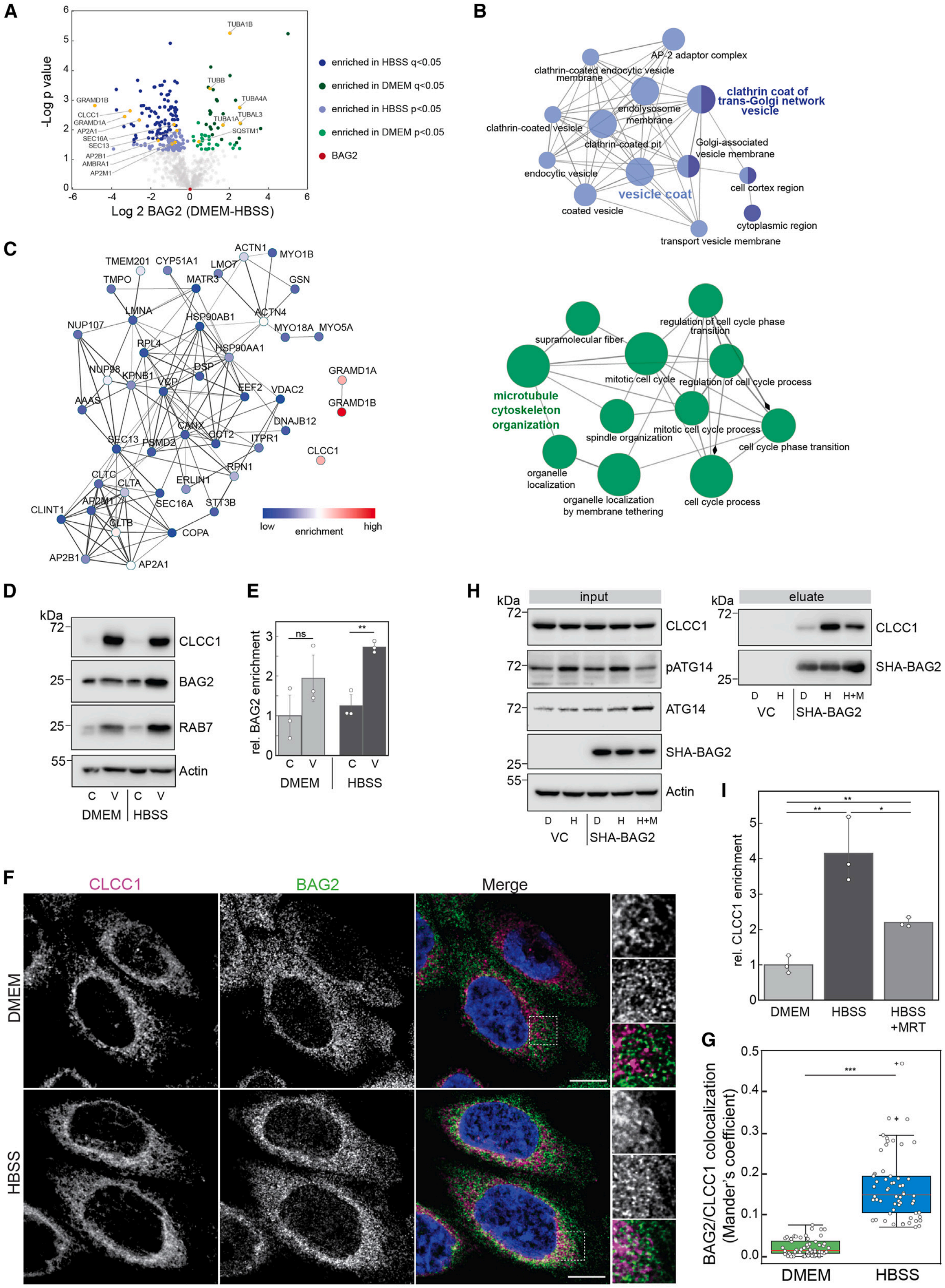

(legend on next page)

variants also reveal a significantly increased co-localization between BAG2^{S31E} and CLCC1 under starvation conditions, in contrast to BAG2^{S31A} (Figures 7F and 7G). These data imply that ULK1 phosphorylation of BAG2 at Ser31 regulates its interaction with the transmembrane protein CLCC1, which reflects a ULK1-dependent change in subcellular localization.

Finally, we also analyzed whether the BAG2 variants differentially affect the observed autophagy phenotype in *BAG2* KO cells. In starvation conditions, expression of *BAG2*^{S31E} but not *BAG2*^{S31A} leads to increased autophagy flux compared to *BAG2*^{WT}as analyzed by LC3-II and GABARAP-II lipidation (Figures 7H–7J). This is also supported by an increased localization of AMBRA1 to the ER membrane in cells expressing *BAG2*^{S31E}, in contrast to cells expressing *BAG2*^{S31A} or *BAG2*^{WT} (Figures 7K–7M). Thus, ULK1 phosphorylation of BAG2 at Ser31 supports localization of BAG2 and AMBRA1 to ER membranes conveying a positive effect to autophagy activity.

DISCUSSION

Autophagy is a vital catabolic pathway, its dysregulation being implicated in numerous human diseases.[2] The ULK1 kinase complex is crucial for canonical autophagy regulation and represents an interesting drug target, which might support the specific modulation of autophagy in diverse disease settings.[77] Here, we present a deep ULK1 interactome using a combination of AP-MS- and PL-MS-based proteomics. By employing N- and C-terminal-tagged protein variants, we characterize 317 high-confidence subunit-specific and common ULK1-complex interactors. Focusing on BAG2, a common interactor that binds to more than one subunit and is identified by AP- and PL-MS, we characterize it as a ULK1 effector that modulates functional autophagy by regulating the subcellular localization of AMBRA1.

AP- and PL-MS are orthogonal approaches that commonly lead to the identification of different sets of target proteins.[38,41] Also in the current study, the overlap between interactors identified by AP- and PL-MS is rather small. The presented deep ULK1-complex interactome is a rich resource for research groups interested in autophagy and its regulation. We highlight the interaction with other protein and lipid kinases and phosphatases, leading to the interpretation that the ULK1 complex forms a signalosome. This is further supported by the observation that autophagy initiation leads to clustering of ULK1-complex members at ER subcompartments, which is observable by IF, i.e., ULK1 or ATG13 puncta formation at omegasomes.[15,78] In agreement, it was recently shown that under starvation conditions ULK1 forms large clusters at the ER containing more than 100 molecules.[79] Interestingly, we identify several SARs as common ULK1-complex interactors under starvation conditions. Nutrient starvation, in our case the lack of amino acids, growth factors, and lipids (the only remaining energy source being glucose), is the classical stimulus for non-selective bulk autophagy. The enrichment of SARs implies that selective autophagy subpathways are also active under “bulk” starvation conditions. Indeed, non-selective bulk autophagy could also be envisioned as the sum of many selective autophagy pathways happening in concert.[80–82] Time-resolved, detailed characterizations of molecular events and autophagosomal proteome compositions are needed to further disentangle selective from potential bulk pathways.[83]

We characterized the HSP70 co-chaperone BAG2 as a direct ULK1 interactor and analyzed the events that govern its function in autophagy in molecular detail. In contrast to other members of the BAG protein family,[22] the primary function of BAG2 appears to be the inhibition of autophagy under basal growth conditions, as its acute depletion by shRNA-based KD leads to increased autophagy flux. The increased flux is due to increased autophagosome nucleation sites as indicated by WIPI2 puncta formation. The increased number of WIPI2 puncta under basal conditions also indicates that the inhibitory function of BAG2 is likely independent of ULK1 activity. In KO cells, the phenotype is more complex: in agreement with the observations in KD cells, increased lipidation of ATG8 proteins and increased WIPI2 puncta numbers are observed; however, in contrast to the effect of acute reduction of BAG2 abundance by shRNA, the chronic reduction of BAG2 levels by KO leads to reduced autophagy flux as analyzed by western blot, MS, and IF. The latter appears to be an indirect effect due to perturbation of lysosomal targeting related to loss of BAG2, as shown by reduced co-localization of p62 and LAMP2. Indeed, we identify BAG2 interacting with

Figure 5. Upon starvation, BAG2 changes its subcellular localization

(A) BAG2 interactome under growth (DMEM) and starvation (HBSS) conditions. HeLa cells inducibly expressing SHA-tagged BAG2 in comparison to vector control were used to determine stimulus-specific interaction partners by AP-MS. Proteins being significantly enriched compared to negative controls were analyzed on differential binding ($n = 3$ biological replicates each; Student‘s t test, unpaired; $p < 0.05$, see panel for details).

(B) BAG2 binds to proteins of endomembranes in starvation and to microtubular proteins in growth conditions. GO enrichment analysis of significant BAG2 interactors. Color code indicates conditions shown in (A).

(C) Protein interaction network of starvation-specific BAG2 interactors. Color scale indicates level of enrichment.

(D and E) Increased BAG2 abundance in microvesicular cell fraction under starvation. Cells were starved for 2 h (HBSS) or kept in growth conditions (DMEM), lysed by douncing, and fractionated into cytosol (C) and 17,000 × *g* microvesicular fraction (V). In $n = 3$ biological replicates, a significant increase of BAG2 in the microvesicular fraction under HBSS conditions is observed. $^{**}p < 0.01$, t test. Single values are highlighted as white dots. Error bars indicate SD.

(F and G) Starvation increases the pool of ER-localized BAG2. BAG2 co-localization with CLCC1 increases upon starvation. (F) IF micrographs from untreated (DMEM) or starved (HBSS, 3 h) HeLa WT cells. Representative pictures of $n = 3$ biological replicates are shown. Scale bars, 10 μm. (G) Co-localization quantification of (F). White dots represent the thresholded Mander’s B coefficient per cell of a total of 60 cells of $n = 3$ biological replicates, corresponding to the fraction of CLCC1 signal co-localizing with the BAG2 signal. A two-way ANOVA test followed by Tukey’s HSD post hoc test was used to identify significant differences. $^{***}p \leq 0.001$.

(H and I) (H) Treatment with 20 μM of the ULK1 inhibitor MRT68921 (after 2 h prior HBSS treatment, total of 4 h) partially blocks the BAG2-CLCC1 interaction. Representative biological replicate of $n = 3$. Samples were normalized to protein amount prior to analysis. (I) Quantification of replicates shown in (H) normalized to BAG2 levels. $^{*}p < 0.05$, $^{**}p < 0.01$, t test. Single values are highlighted as white dots. Error bars indicate 95% confidence interval.

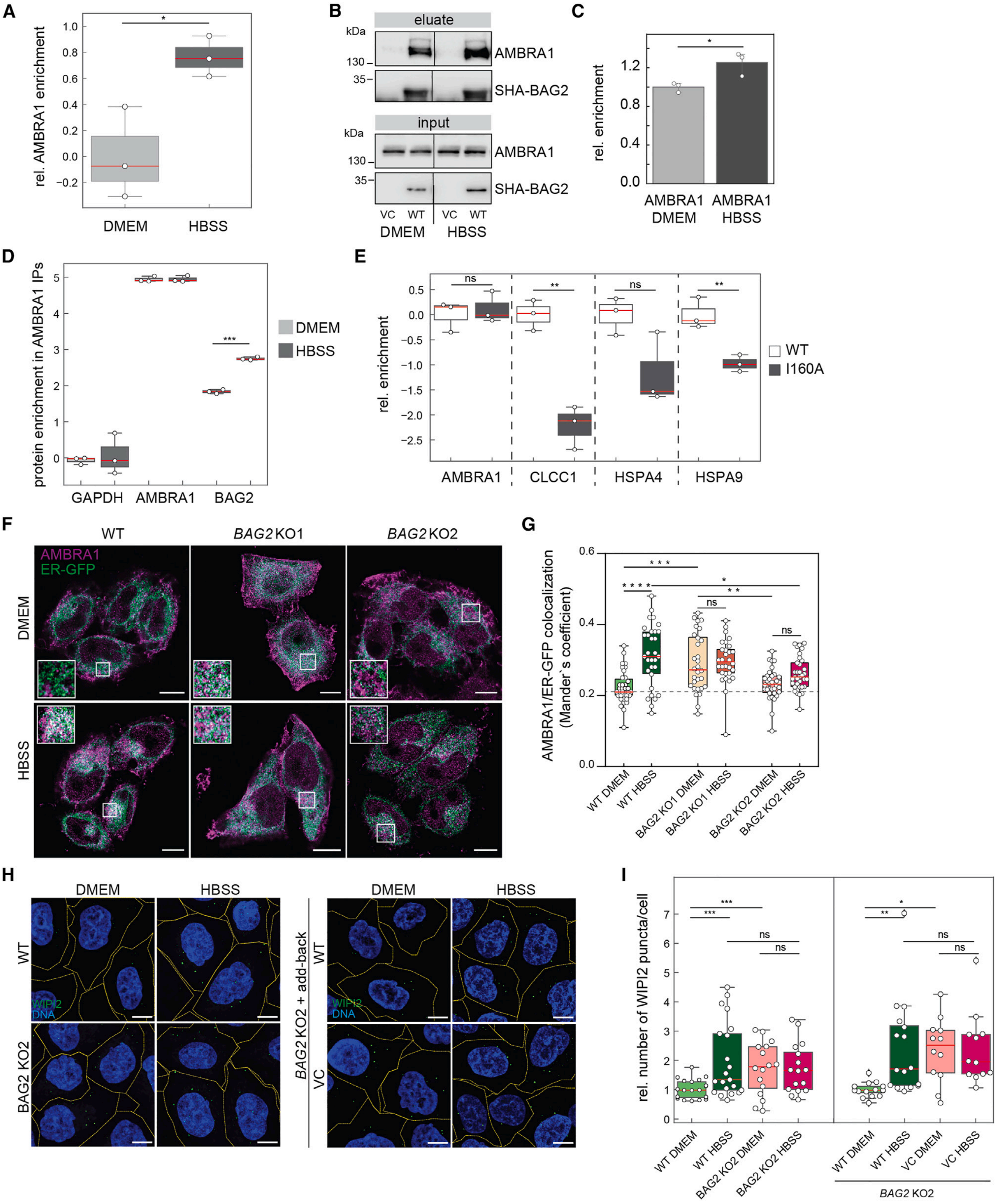

(legend on next page)

several vesicle coat proteins: clathrin-coat proteins such as adapter protein complex 2 members AP2A1, B1, and M1, which are important for clathrin-coated vesicle formation and cargo selectivity,[84] and COPII coat proteins such as SEC13.

Under starvation conditions and activation of ULK1, BAG2 changes its protein interactions and with this its subcellular localization in a ULK1-dependent manner, localizing more to endomembranes, as exemplified by binding more strongly to the ER-/Golgi-resident transmembrane protein CLCC1. In a recent spatial proteomics approach, BAG2 was identified as localizing to SEC16A-positive ERES,[85] which are involved in autophagosome biogenesis.[86,87] Our data recapitulate this finding by additionally implying that BAG2 may localize to different membrane subcompartments, which would support the interpretation that BAG2 may fulfill multiple functions important for autophagy activity. As the *Caenorhabditis elegans* homologs of BAG2 and HSC70 have been shown to regulate intracellular protein localization,[88] we hypothesize that the change in BAG2 localization likely also affects BAG2 client proteins. One autophagy-relevant client of BAG2 that is identified in the current study is AMBRA1.

KO and KD of BAG2 support increased AMBRA1 localization to the ER membrane. The increase in WIPI2 puncta in both KO and KD cells is in agreement with ER-localized AMBRA1, as their formation is PI3P dependent, reflecting an increase in VPS34 kinase activity.[73,74] Whether the increase in autophagosome initiation sites in BAG2-depleted cells represents ER-connected phagophores or accumulated ATG9 vesicles will have to be addressed in future studies.[89–91] The change in BAG2 localization is directly regulated by ULK1, as pharmacological and genetic inhibition of ULK1 decreases and mutating the ULK1 target site $BAG2^{Ser31}$ to a phosphomimetic glutamic acid increases CLCC1 binding, respectively. The respective alanine mutation does not have a strong effect. Indeed, by using *in vivo* and *in vitro* phosphoproteomics, we show that $BAG2^{Ser31}$ is a bona fide ULK1 target site.

The synonym of AMBRA1 is DCAF3 (DDB1- and CUL4-associated factor 3), as AMBRA1 has also been identified as a binding partner of E3 ubiquitin ligases, among them Cullin 4 and Cullin 5,[92,93] TRAF6,[94] and TRIM32.[95] AMBRA1 and ULK1 appear to be linked by feedback, ULK1 phosphorylating AMBRA1,[71] which in turn supports the TRAF6-dependent ubiquitination and stabilization of ULK1.[94] We cannot exclude that AMBRA1 affects the ubiquitination of BAG2 and along with this its stability or protein-protein interactions, affecting potentially both autophagosomal and proteasomal protein degradation. This issue will have to be addressed in the future.

Taken together, in the current study we generated a deep ULK1 complex interactome highlighting that the holo-complex forms an elaborate signalosome. By phosphorylating the co-chaperone BAG2, ULK1 modulates its subcellular localization, positively affecting autophagy initiation in response to stress by stabilizing AMBRA1 at the ER membrane. However, next to regulation of autophagy initiation, the ULK1 holo-complex appears to modulate adaptation to limited nutrient supply in general. SARs are important binding partners of ULK1-complex members, indicating the activation of starvation-dependent selective autophagy pathways and questioning the relevance of non-specific bulk degradation by autophagy in response to stress.

Limitations of the study

The contrasting phenotypes of BAG2 KO and KD cells with respect to autophagy activity highlight several limitations of the current study that will have to be addressed in the future. BAG2 appears to have a general effect on vesicle formation and/or trafficking affecting (1) autophagosome biogenesis via AMBRA1 localization and (2) autophagosome turnover, potentially in an indirect manner, by interacting with several vesicle

Figure 6. BAG2 regulates the subcellular distribution of AMBRA1

(A) AMBRA1 binds more strongly to SHA-BAG2 under starvation conditions. Shown is the relative enrichment of AMBRA1 in BAG2-AP as determined by MS of $n = 3$ biological replicates. Boxplots show spreads of $\log_2$-transformed MS ratios compared to negative controls. Single values are highlighted as white dots. Error bars indicate 95% confidence intervals.

(B and C) AMBRA1 binds more strongly to SHA-BAG2 under starvation conditions as determined by AP-western blot analysis. (B) One representative of $n = 3$ biological replicates. Samples were normalized to protein amount prior to analysis. Samples were run on one gel, and black lines indicate cropping of unrelated lanes; these data were also used to generate Figures 3B and 7D. (C) Quantification of replicates shown in (B). $^*p < 0.05$, t test. Error bars indicate 95% confidence interval.

(D) Endogenous AMBRA1 and BAG2 interact. Shown are relative abundances of annotated proteins in AMBRA1 immunoprecipitation (IP)-MS experiments. Starvation (1 h HBSS) leads to an increase in AMBRA1-BAG2 interaction as compared to growth conditions (DMEM). GAPDH is shown as negative control. Boxplot shows $\log_2$-transformed relative fold changes of protein abundances (iBAQ values) compared to immunoglobulin G controls normalized to AMBRA1 enrichment. Error bars indicate 95% confidence interval. Single values of $n = 3$ biological replicates are highlighted as white dots. $^{***}p < 0.001$, t test.

(E) The interaction of AMBRA1 with BAG2 does not depend on HSC/HSP70 binding. Shown are relative abundances of annotated proteins in SHA-BAG2 AP-MS experiments. Compared to $BAG2^{WT}$ (WT), $BAG2^{I160A}$ (I160A) interacts less with CLCC1, HSPA4, and HSPA9. The interaction with AMBRA1 is not perturbed by the point mutation. Boxplots show $\log_2$-transformed relative fold changes of protein abundances (iBAQ values) normalized to WT. Error bars indicate 95% confidence interval. Single values of $n = 3$ biological replicates are highlighted as white dots. $^{**}p < 0.01$; ns, not significant; t test.

(F and G) Loss of BAG2 leads to perturbed recruitment of AMBRA1 to ER membrane. (F) Representative fluorescence images of ER-GFP expressing HeLa WT and *BAG2* KO cells stained for AMBRA1 (Alexa 647) and subjected, or not, to nutrient deprivation (HBSS, 2 h). Scale bars, 5 μm. (G) Quantitative analysis of the fraction of AMBRA1 signal co-localizing with ER-GFP per cell is reported as the mean ± SD, $n = 30$ cells per condition; $^*p \leq 0.05$, $^{**}p \leq 0.005$, $^{***}p \leq 0.0005$ using a two-way ANOVA test followed by Tukey's HSD post hoc test.

(H and I) Loss of BAG2 leads to increased number of WIPI2 dots. (H) WIPI2 puncta analysis using IF micrographs from untreated (DMEM) or starved (HBSS, 3 h) HeLa WT and *BAG2* KO cells (left panels) or *BAG2* KO cells transfected with a lentiviral control vector (VC) or a vector encoding $BAG2^{WT}$ (WT) (right panels). Representative pictures of $n = 3$ biological replicates are shown. Scale bars, 10 μm. (I) Puncta quantification of (H). White dots represent the quantified average WIPI2 puncta per cell per image (5–23 cells per image, with a total of 12 images of $n = 3$ biological replicates for *BAG2* KO + VC samples, or 16 images of $n = 4$ biological replicates for each other condition). A two-way ANOVA test followed by Tukey's HSD post hoc test was used to identify significant differences. $^*p < 0.05$, $^{**}p < 0.01$, $^{***}p < 0.001$; ns, not significant.

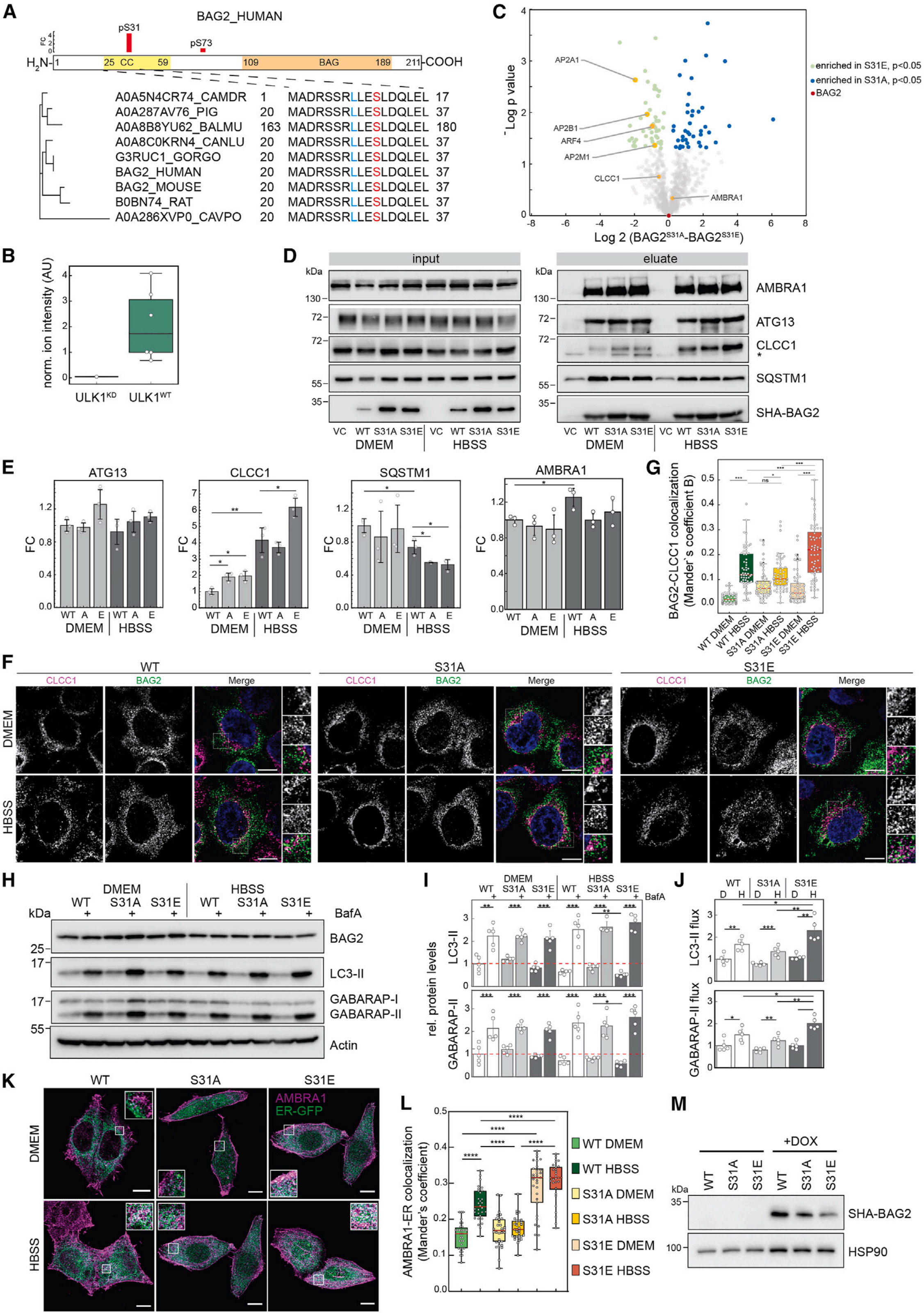

(legend on next page)

coat proteins. Further studies are needed to fully uncover the role of BAG2 in intracellular vesicle trafficking, fusion, and lysosomal activity. By employing the variant BAG2^{I160A}, which does not interact with HSC70 proteins, we could discriminate between CLCC1 and AMBRA1 binding. However, we do not know whether binding to CLCC1 is of functional relevance, as we employed this protein merely as an ER marker. The distinct interactions of BAG2 with these two proteins and the lack of detecting AMBRA1 in CLCC1 IPs and vice versa raises the question of whether multiple, distinct BAG2 complexes exist at the ER membrane. Interestingly, the effects of *BAG2^{S31E}* expression and starvation seem to be additive with respect to CLCC1 binding, implying that the interaction does not solely rely on Ser31 phosphorylation. Additional amino acids of BAG2 or CLCC1 might be modified in the tested condition affecting binding, either via phosphorylation by ULK1 or other kinases, or via additional post-translational modifications, potentially also affecting AMBRA1 binding. The fact that the BAG2-CLCC1 interaction is also dependent on HSC70 binding further supports the interpretation that next to Ser31 phosphorylation additional mechanisms affect this interaction. Further studies are needed to characterize the regulation of BAG2 and the immediate effect of BAG2 Ser31 phosphorylation. It is also not clear how the interaction between AMBRA1 and BAG2 is regulated on a molecular level and whether it occurs at several subcellular localizations. Whereas our interactome studies indicate a microtubular localization, IF analyses exhibit an intricate staining, highlighting that both BAG2 and AMBRA1 localize to numerous subcellular locations.

RESOURCE AVAILABILITY

Lead contact

Further information and requests for resources and reagents should be directed to and will be fulfilled by the lead contact, Jörn Dengjel (joern.dengjel@unifr.ch).

Materials availability

All unique/stable reagents generated in this study are available from the lead contact without restriction.

Data and code availability

- Proteomics data is freely available via the PRIDE repository (https://www.ebi.ac.uk/pride/), data identifier PXD044974.
- This paper does not report original code.
- Any additional information required to reanalyze the data reported in this paper is available from the lead contact upon request.

ACKNOWLEDGMENTS

This work was supported by the Canton and the University of Fribourg as part of the SKINTEGRITY.CH collaborative research project and by the Swiss National Science Foundation (grants 310030_212187, 310030_184781 to J.D., grant 310030_192614 to W.J.K.). This work has been also supported by grants from the Italian Ministry of Health (Ricerca Corrente e Finalizzata, PNRR-MAD-2022-12375755 to G.M.F. and GR-2019-12369231 to M.A.), and from CAPES, Coordenação de Aperfeiçoamento de Pessoal de Nível Superior – Brasil (Código de Financiamento 001) for a scholarship to L.d.O.M. We acknowledge co-funding from Next Generation EU through the Italian Ministry of University and Research, in the context of the National Recovery and Resilience Plan, Investment PE8 – Project Age-It: "Aging Well in an Aging Society" to G.M.F., co-financed by the Next Generation EU (DM 1557 11.10.2022) CUP B53C22004090006. We would like to thank Prof. Mario Tschan, Dr. Anna Bill, and Dr. Jun Xu for support with FACS analysis. We thank Dr. Rudolf Rohr for support with the statistical analyses.

AUTHOR CONTRIBUTIONS

Conceptualization, D.S.S., S.K.-P., and J.D.; data curation, D.S.S., S.K.-P., and J.D.; formal analysis, D.S.S., S.K.-P., C.V., S.F., L.d.O.M., B.P., M.S., M.A., and J.D.; funding acquisition, W.J.K., D.K., M.A., G.M.F., and J.D.; investigation, D.S.S., S.K.-P., C.V., S.F., L.d.O.M., B.P., M.S., and M.A.; resources, J.Z., W.J.K., M.A., D.K., G.M.F., and J.D.; supervision, S.K.-P., W.J.K., M.A., D.K., G.M.F., and J.D.; visualization, D.S.S., C.V., S.K.-P., and J.D.; writing – original draft, D.S.S., S.K.-P., and J.D.; writing – review and editing, all authors.

Figure 7. BAG2 is a ULK1 target, its phosphorylation affecting localization and protein-protein interactions
(A) BAG2^{Ser31} is an *in vivo* ULK1 target site. Ser31 was identified as being significantly phosphorylated in MEFs expressing human ULK1 compared to *ULK1* KO MEFs, in contrast to Ser73, which did not differ depending on the ULK1 status.[54] Red bars indicate fold change of phosphorylation ($n \geq 2$ biological replicates). Ser31 lies within a ULK1 consensus motif, which is highly conserved in mammals. CAMDR, *Camelus dromedarius*, Arabian camel; PIG, *Sus scrofa*, pig; BALMU, *Balaenoptera musculus*, blue whale; CANLU, *Canis lupus*, gray wolf; GORGO, *Gorilla gorilla*, gorilla (Western lowland gorilla); CAVPO, *Cavia porcellus*, guinea pig.
(B) BAG2^{Ser31} is phosphorylated by WT ULK1 (ULK1^{WT}) *in vitro*, but not by kinase-dead ULK1 (ULK1^{KD}); $n = 6$ biological replicates.
(C–E) BAG2^{Ser31} status affects BAG2-protein interactions. (C) Volcano plot of AP-MS data highlighting differential binding of BAG2^{Ser31} variants. (D) CoIP western blot of SHA-tagged WT-, S31A-, and S31E-BAG2 variants. Shown is one representative of $n = 3$ biological replicates; these data were also used to generate Figures 3B and 6B. (E) Quantification of replicates shown in (D). Samples were normalized to protein amount prior to analysis. Error bars indicate 95% confidence interval. Single values are highlighted as white dots. *$p < 0.05$, **$p < 0.01$, unpaired t test.
(F and G) (F) Expression of BAG2^{S31E} in *BAG2* KO cells leads to a significant increase in co-localization of BAG2 and CLCC1 compared to BAG2^{WT} and BAG2^{S31A} expressing KO cells in starvation conditions (3 h, HBSS) as analyzed by IF. Representative pictures of $n = 3$ biological replicates are shown. Scale bars, 10 μm. (G) Data of $n = 3$ biological replicates each, 20 cells per replicate. White dots represent the thresholded Mander's B coefficient per cell of a total of 60 cells, corresponding to the fraction of CLCC1 signal co-localizing with the BAG2 signal. A two-way ANOVA test followed by Tukey's HSD post hoc test was used to identify significant differences. *$p < 0.05$, ***$p < 0.001$; ns, not significant.
(H–J) Cells expressing BAG2^{S31E} exhibit an increased autophagy flux in starvation compared to BAG2^{WT} and BAG2^{S31A} expressing cells. (H) Representative western blots of $n = 5$ biological replicates. Actin serves as loading control. (I) Quantifications of blots shown in (H). Red dotted lines indicate protein levels in DMEM control conditions. (J) Comparing BafA1-treated with non-treated lanes indicates increased autophagy flux in starvation (HBSS, H) compared to growth conditions (DMEM, D). BAG2^{S31E} leads to a significant increase in autophagy flux in starvation compared to BAG2^{WT} and BAG2^{S31A}. Student's t test, unpaired; *$p < 0.05$, **$p < 0.01$, ***$p < 0.001$. Single values are highlighted as white dots. Error bars indicate 95% confidence interval.
(K) Representative fluorescence images of ER-GFP expressing HeLa BAG2 KO that were re-introduced with BAG2^{WT}, BAG2^{S31A}, or BAG2^{S31E}; cells were stained for AMBRA1 (Alexa 647) and subjected, or not, to nutrient deprivation, adding HBSS for 2 h. Scale bars, 10 μm.
(L) Quantitative analysis of the fraction of AMBRA1 signal co-localizing with ER-GFP per cell is reported as the mean ± SD, $n = 30$ cells per condition; *$p \leq 0.05$, **$p \leq 0.005$, ***$p \leq 0.0005$ using a two-way ANOVA test followed by Tukey's HSD post hoc test.
(M) Western blot analysis of SHA-BAG2 WT and mutants re-expressed in *BAG2* KO2 HeLa cells from data reported in (K).

DECLARATION OF INTERESTS

The authors declare no competing interests.

STAR★METHODS

Detailed methods are provided in the online version of this paper and include the following:

- KEY RESOURCES TABLE
- EXPERIMENTAL MODEL AND STUDY PARTICIPANT DETAILS
- METHOD DETAILS
    - ○ Cloning of recombinant DNA constructs
    - ○ Cloning of CRISPR Cas-9 knockout vectors and cell line generation
    - ○ Lentivirus production and infection of target cells
    - ○ Antibodies
    - ○ Immunostainings and florescence microscopy analysis
    - ○ Cell lysis
    - ○ Immunoblotting
    - ○ Whole proteome analyses
    - ○ Cell fractionation
    - ○ HA affinity purification and MS sample preparation
    - ○ Proximity labeling and streptavidin-based affinity purifications
    - ○ Mass spectrometry-based proteomic analyses
    - ○ Halo-LC3 assays
    - ○ Yeast two-hybrid (Y2H) interaction analysis
- QUANTIFICATION AND STATISTICAL ANALYSIS
    - ○ MS quantification and statistical analysis

SUPPLEMENTAL INFORMATION

Supplemental information can be found online at https://doi.org/10.1016/j.celrep.2024.114689.

Received: January 8, 2024
Revised: June 15, 2024
Accepted: August 12, 2024

REFERENCES

1. Yamamoto, H., Zhang, S., and Mizushima, N. (2023). Autophagy genes in biology and disease. Nat. Rev. Genet. *24*, 382–400. https://doi.org/10.1038/s41576-022-00562-w.
2. Klionsky, D.J., Petroni, G., Amaravadi, R.K., Baehrecke, E.H., Ballabio, A., Boya, P., Bravo-San Pedro, J.M., Cadwell, K., Cecconi, F., Choi, A.M.K., et al. (2021). Autophagy in major human diseases. EMBO J. *40*, e108863. https://doi.org/10.15252/embj.2021108863.
3. Hu, Y., and Reggiori, F. (2022). Molecular regulation of autophagosome formation. Biochem. Soc. Trans. *50*, 55–69. https://doi.org/10.1042/BST20210819.
4. Delorme-Axford, E., and Klionsky, D.J. (2018). Transcriptional and post-transcriptional regulation of autophagy in the yeast Saccharomyces cerevisiae. J. Biol. Chem. *293*, 5396–5403. https://doi.org/10.1074/jbc.R117.804641.
5. Licheva, M., Raman, B., Kraft, C., and Reggiori, F. (2022). Phosphoregulation of the autophagy machinery by kinases and phosphatases. Autophagy *18*, 104–123. https://doi.org/10.1080/15548627.2021.1909407.
6. Abeliovich, H., Dunn, W.A., Jr., Kim, J., and Klionsky, D.J. (2000). Dissection of autophagosome biogenesis into distinct nucleation and expansion steps. J. Cell Biol. *151*, 1025–1034. https://doi.org/10.1083/jcb.151.5.1025.
7. Chan, E.Y.W., Kir, S., and Tooze, S.A. (2007). siRNA screening of the kinome identifies ULK1 as a multidomain modulator of autophagy. J. Biol. Chem. *282*, 25464–25474. https://doi.org/10.1074/jbc.M703663200.
8. Young, A.R.J., Chan, E.Y.W., Hu, X.W., Köchl, R., Crawshaw, S.G., High, S., Hailey, D.W., Lippincott-Schwartz, J., and Tooze, S.A. (2006). Starvation and ULK1-dependent cycling of mammalian Atg9 between the TGN and endosomes. J. Cell Sci. *119*, 3888–3900. https://doi.org/10.1242/jcs.03172.
9. Chan, E.Y.W., Longatti, A., McKnight, N.C., and Tooze, S.A. (2009). Kinase-inactivated ULK proteins inhibit autophagy via their conserved C-terminal domains using an Atg13-independent mechanism. Mol. Cell Biol. *29*, 157–171. https://doi.org/10.1128/MCB.01082-08.
10. Hosokawa, N., Hara, T., Kaizuka, T., Kishi, C., Takamura, A., Miura, Y., Iemura, S.i., Natsume, T., Takehana, K., Yamada, N., et al. (2009). Nutrient-dependent mTORC1 association with the ULK1-Atg13-FIP200 complex required for autophagy. Mol. Biol. Cell *20*, 1981–1991. https://doi.org/10.1091/mbc.E08-12-1248.
11. Mercer, C.A., Kaliappan, A., and Dennis, P.B. (2009). A novel, human Atg13 binding protein, Atg101, interacts with ULK1 and is essential for macroautophagy. Autophagy *5*, 649–662. https://doi.org/10.4161/auto.5.5.8249.
12. Hosokawa, N., Sasaki, T., Iemura, S.i., Natsume, T., Hara, T., and Mizushima, N. (2009). Atg101, a novel mammalian autophagy protein interacting with Atg13. Autophagy *5*, 973–979. https://doi.org/10.4161/auto.5.7.9296.
13. Hara, T., Takamura, A., Kishi, C., Iemura, S.I., Natsume, T., Guan, J.L., and Mizushima, N. (2008). FIP200, a ULK-interacting protein, is required for autophagosome formation in mammalian cells. J. Cell Biol. *181*, 497–510. https://doi.org/10.1083/jcb.200712064.
14. Shi, X., Yokom, A.L., Wang, C., Young, L.N., Youle, R.J., and Hurley, J.H. (2020). ULK complex organization in autophagy by a C-shaped FIP200 N-terminal domain dimer. J. Cell Biol. *219*, e201911047. https://doi.org/10.1083/jcb.201911047.
15. Karanasios, E., Walker, S.A., Okkenhaug, H., Manifava, M., Hummel, E., Zimmermann, H., Ahmed, Q., Domart, M.C., Collinson, L., and Ktistakis, N.T. (2016). Autophagy initiation by ULK complex assembly on ER tubulovesicular regions marked by ATG9 vesicles. Nat. Commun. *7*, 12420. https://doi.org/10.1038/ncomms12420.
16. Mercer, T.J., Gubas, A., and Tooze, S.A. (2018). A molecular perspective of mammalian autophagosome biogenesis. J. Biol. Chem. *293*, 5386–5395. https://doi.org/10.1074/jbc.R117.810366.
17. Mercer, T.J., Ohashi, Y., Boeing, S., Jefferies, H.B.J., De Tito, S., Flynn, H., Tremel, S., Zhang, W., Wirth, M., Frith, D., et al. (2021). Phosphoproteomic identification of ULK substrates reveals VPS15-dependent ULK/VPS34 interplay in the regulation of autophagy. EMBO J. *40*, e105985. https://doi.org/10.15252/embj.2020105985.
18. Behrends, C., Sowa, M.E., Gygi, S.P., and Harper, J.W. (2010). Network organization of the human autophagy system. Nature *466*, 68–76. https://doi.org/10.1038/nature09204.
19. Joo, J.H., Wang, B., Frankel, E., Ge, L., Xu, L., Iyengar, R., Li-Harms, X., Wright, C., Shaw, T.I., Lindsten, T., et al. (2016). The Noncanonical Role of ULK/ATG1 in ER-to-Golgi Trafficking Is Essential for Cellular Homeostasis. Mol. Cell *62*, 491–506. https://doi.org/10.1016/j.molcel.2016.04.020.
20. Siva Sankar, D., and Dengjel, J. (2021). Protein complexes and neighborhoods driving autophagy. Autophagy *17*, 2689–2705. https://doi.org/10.1080/15548627.2020.1847461.
21. Takayama, S., and Reed, J.C. (2001). Molecular chaperone targeting and regulation by BAG family proteins. Nat. Cell Biol. *3*, E237–E241. https://doi.org/10.1038/ncb1001-e237.
22. Pattingre, S., and Turtoi, A. (2022). BAG Family Members as Mitophagy Regulators in Mammals. Cells *11*, 681. https://doi.org/10.3390/cells11040681.
23. Kabbage, M., and Dickman, M.B. (2008). The BAG proteins: a ubiquitous family of chaperone regulators. Cell. Mol. Life Sci. *65*, 1390–1402. https://doi.org/10.1007/s00018-008-7535-2.

24. Munthe, L.A., Blichfeldt, E., Sollien, A., Dembic, Z., and Bogen, B. (1996). T cells with two Tcrbeta chains and reactivity to both MHC/idiotypic peptide and superantigen. Cell. Immunol. *170*, 283–290. https://doi.org/10.1006/cimm.1996.0162.
25. Qu, D., Hage, A., Don-Carolis, K., Huang, E., Joselin, A., Safarpour, F., Marcogliese, P.C., Rousseaux, M.W.C., Hewitt, S.J., Huang, T., et al. (2015). BAG2 Gene-mediated Regulation of PINK1 Protein Is Critical for Mitochondrial Translocation of PARKIN and Neuronal Survival. J. Biol. Chem. *290*, 30441–30452. https://doi.org/10.1074/jbc.M115.677815.
26. Arndt, V., Daniel, C., Nastainczyk, W., Alberti, S., and Höhfeld, J. (2005). BAG-2 acts as an inhibitor of the chaperone-associated ubiquitin ligase CHIP. Mol. Biol. Cell *16*, 5891–5900. https://doi.org/10.1091/mbc.e05-07-0660.
27. de Paula, C.A.D., Santiago, F.E., de Oliveira, A.S.A., Oliveira, F.A., Almeida, M.C., and Carrettiero, D.C. (2016). The Co-chaperone BAG2 Mediates Cold-Induced Accumulation of Phosphorylated Tau in SH-SY5Y Cells. Cell. Mol. Neurobiol. *36*, 593–602. https://doi.org/10.1007/s10571-015-0239-x.
28. Che, X., Tang, B., Wang, X., Chen, D., Yan, X., Jiang, H., Shen, L., Xu, Q., Wang, G., and Guo, J. (2013). The BAG2 protein stabilises PINK1 by decreasing its ubiquitination. Biochem. Biophys. Res. Commun. *441*, 488–492. https://doi.org/10.1016/j.bbrc.2013.10.086.
29. Ragimbeau, R., El Kebriti, L., Sebti, S., Fourgous, E., Boulahtouf, A., Arena, G., Espert, L., Turtoi, A., Gongora, C., Houédé, N., and Pattingre, S. (2021). BAG6 promotes PINK1 signaling pathway and is essential for mitophagy. FASEB J *35*, e21361. https://doi.org/10.1096/fj.202000930R.
30. Tahrir, F.G., Knezevic, T., Gupta, M.K., Gordon, J., Cheung, J.Y., Feldman, A.M., and Khalili, K. (2017). Evidence for the Role of BAG3 in Mitochondrial Quality Control in Cardiomyocytes. J. Cell. Physiol. *232*, 797–805. https://doi.org/10.1002/jcp.25476.
31. Liang, S., Wang, F., Bao, C., Han, J., Guo, Y., Liu, F., and Zhang, Y. (2020). BAG2 ameliorates endoplasmic reticulum stress-induced cell apoptosis in Mycobacterium tuberculosis-infected macrophages through selective autophagy. Autophagy *16*, 1453–1467. https://doi.org/10.1080/15548627.2019.1687214.
32. Antonioli, M., Di Rienzo, M., Piacentini, M., and Fimia, G.M. (2017). Emerging Mechanisms in Initiating and Terminating Autophagy. Trends Biochem. Sci. *42*, 28–41. https://doi.org/10.1016/j.tibs.2016.09.008.
33. Wang, B., Maxwell, B.A., Joo, J.H., Gwon, Y., Messing, J., Mishra, A., Shaw, T.I., Ward, A.L., Quan, H., Sakurada, S.M., et al. (2019). ULK1 and ULK2 Regulate Stress Granule Disassembly Through Phosphorylation and Activation of VCP/p97. Mol. Cell *74*, 742–757.e8. https://doi.org/10.1016/j.molcel.2019.03.027.
34. Tu, Y.X.I., Sydor, A.M., Coyaud, E., Laurent, E.M.N., Dyer, D., Mellouk, N., St-Germain, J., Vernon, R.M., Forman-Kay, J.D., Li, T., et al. (2022). Global Proximity Interactome of the Human Macroautophagy Pathway. Autophagy *18*, 1174–1186. https://doi.org/10.1080/15548627.2021.1965711.
35. Goodwin, J.M., Dowdle, W.E., DeJesus, R., Wang, Z., Bergman, P., Kobylarz, M., Lindeman, A., Xavier, R.J., McAllister, G., Nyfeler, B., et al. (2017). Autophagy-Independent Lysosomal Targeting Regulated by ULK1/2-FIP200 and ATG9. Cell Rep. *20*, 2341–2356. https://doi.org/10.1016/j.celrep.2017.08.034.
36. Nguyen, A., Lugarini, F., David, C., Hosnani, P., Alagöz, Ç., Friedrich, A., Schlütermann, D., Knotkova, B., Patel, A., Parfentev, I., et al. (2023). Metamorphic proteins at the basis of human autophagy initiation and lipid transfer. Mol. Cell *83*, 2077–2090.e12. https://doi.org/10.1016/j.molcel.2023.04.026.
37. Branon, T.C., Bosch, J.A., Sanchez, A.D., Udeshi, N.D., Svinkina, T., Carr, S.A., Feldman, J.L., Perrimon, N., and Ting, A.Y. (2018). Efficient proximity labeling in living cells and organisms with TurboID. Nat. Biotechnol. *36*, 880–887. https://doi.org/10.1038/nbt.4201.
38. Liu, X., Salokas, K., Weldatsadik, R.G., Gawriyski, L., and Varjosalo, M. (2020). Combined proximity labeling and affinity purification-mass spectrometry workflow for mapping and visualizing protein interaction networks. Nat. Protoc. *15*, 3182–3211. https://doi.org/10.1038/s41596-020-0365-x.
39. Turco, E., Witt, M., Abert, C., Bock-Bierbaum, T., Su, M.Y., Trapannone, R., Sztacho, M., Danieli, A., Shi, X., Zaffagnini, G., et al. (2019). FIP200 Claw Domain Binding to p62 Promotes Autophagosome Formation at Ubiquitin Condensates. Mol. Cell *74*, 330–346.e11. https://doi.org/10.1016/j.molcel.2019.01.035.
40. Qi, S., Kim, D.J., Stjepanovic, G., and Hurley, J.H. (2015). Structure of the Human Atg13-Atg101 HORMA Heterodimer: an Interaction Hub within the ULK1 Complex. Structure *23*, 1848–1857. https://doi.org/10.1016/j.str.2015.07.011.
41. Lambert, J.P., Tucholska, M., Go, C., Knight, J.D.R., and Gingras, A.C. (2015). Proximity biotinylation and affinity purification are complementary approaches for the interactome mapping of chromatin-associated protein complexes. J. Proteomics *118*, 81–94. https://doi.org/10.1016/j.jprot.2014.09.011.
42. Kirkin, V., Lamark, T., Sou, Y.S., Bjørkøy, G., Nunn, J.L., Bruun, J.A., Shvets, E., McEwan, D.G., Clausen, T.H., Wild, P., et al. (2009). A role for NBR1 in autophagosomal degradation of ubiquitinated substrates. Mol. Cell *33*, 505–516. https://doi.org/10.1016/j.molcel.2009.01.020.
43. Smith, M.D., Harley, M.E., Kemp, A.J., Wills, J., Lee, M., Arends, M., von Kriegsheim, A., Behrends, C., and Wilkinson, S. (2018). CCPG1 Is a Non-canonical Autophagy Cargo Receptor Essential for ER-Phagy and Pancreatic ER Proteostasis. Dev. Cell *44*, 217–232.e11. https://doi.org/10.1016/j.devcel.2017.11.024.
44. Newman, A.C., Scholefield, C.L., Kemp, A.J., Newman, M., McIver, E.G., Kamal, A., and Wilkinson, S. (2012). TBK1 kinase addiction in lung cancer cells is mediated via autophagy of Tax1bp1/Ndp52 and non-canonical NF-kappaB signalling. PLoS One *7*, e50672. https://doi.org/10.1371/journal.pone.0050672.
45. Ravenhill, B.J., Boyle, K.B., von Muhlinen, N., Ellison, C.J., Masson, G.R., Otten, E.G., Foeglein, A., Williams, R., and Randow, F. (2019). The Cargo Receptor NDP52 Initiates Selective Autophagy by Recruiting the ULK Complex to Cytosol-Invading Bacteria. Mol. Cell *74*, 320–329.e6. https://doi.org/10.1016/j.molcel.2019.01.041.
46. Zhou, Z., Liu, J., Fu, T., Wu, P., Peng, C., Gong, X., Wang, Y., Zhang, M., Li, Y., Wang, Y., et al. (2021). Phosphorylation regulates the binding of autophagy receptors to FIP200 Claw domain for selective autophagy initiation. Nat. Commun. *12*, 1570. https://doi.org/10.1038/s41467-021-21874-1.
47. Ohnstad, A.E., Delgado, J.M., North, B.J., Nasa, I., Kettenbach, A.N., Schultz, S.W., and Shoemaker, C.J. (2020). Receptor-mediated clustering of FIP200 bypasses the role of LC3 lipidation in autophagy. EMBO J. *39*, e104948. https://doi.org/10.15252/embj.2020104948.
48. Turco, E., Savova, A., Gere, F., Ferrari, L., Romanov, J., Schuschnig, M., and Martens, S. (2021). Reconstitution defines the roles of p62, NBR1 and TAX1BP1 in ubiquitin condensate formation and autophagy initiation. Nat. Commun. *12*, 5212. https://doi.org/10.1038/s41467-021-25572-w.
49. Le Guerroue, F., Bunker, E.N., Rosencrans, W.M., Nguyen, J.T., Basar, M.A., Werner, A., Chou, T.F., Wang, C., and Youle, R.J. (2023). TNIP1 inhibits selective autophagy via bipartite interaction with LC3/GABARAP and TAX1BP1. Mol Cell *83*, 927–941.e928. https://doi.org/10.1016/j.molcel.2023.02.023.
50. Zhou, J., Rasmussen, N.L., Olsvik, H.L., Akimov, V., Hu, Z., Evjen, G., Kaeser-Pebernard, S., Sankar, D.S., Roubaty, C., Verlhac, P., et al. (2023). TBK1 phosphorylation activates LIR-dependent degradation of the inflammation repressor TNIP1. J. Cell Biol. *222*, e202108144. https://doi.org/10.1083/jcb.202108144.
51. Kurusu, R., Fujimoto, Y., Morishita, H., Noshiro, D., Takada, S., Yamano, K., Tanaka, H., Arai, R., Kageyama, S., Funakoshi, T., et al. (2023).

Integrated proteomics identifies p62-dependent selective autophagy of the supramolecular vault complex. Dev. Cell *58*, 1189–1205.e11. https://doi.org/10.1016/j.devcel.2023.04.015.

52. Dowdle, W.E., Nyfeler, B., Nagel, J., Elling, R.A., Liu, S., Triantafellow, E., Menon, S., Wang, Z., Honda, A., Pardee, G., et al. (2014). Selective VPS34 inhibitor blocks autophagy and uncovers a role for NCOA4 in ferritin degradation and iron homeostasis in vivo. Nat. Cell Biol. *16*, 1069–1079. https://doi.org/10.1038/ncb3053.
53. Ishii, S., Chino, H., Ode, K.L., Kurikawa, Y., Ueda, H.R., Matsuura, A., Mizushima, N., and Itakura, E. (2023). CCPG1 recognizes endoplasmic reticulum luminal proteins for selective ER-phagy. Mol. Biol. Cell *34*, ar29. https://doi.org/10.1091/mbc.E22-09-0432.
54. Hu, Z., Sankar, D.S., Vu, B., Leytens, A., Vionnet, C., Wu, W., Stumpe, M., Martínez-Martínez, E., Stork, B., and Dengjel, J. (2021). ULK1 phosphorylation of striatin activates protein phosphatase 2A and autophagy. Cell Rep. *36*, 109762. https://doi.org/10.1016/j.celrep.2021.109762.
55. Sanchez-Martin, P., Kriegenburg, F., Alves, L., Adam, J., Elsaesser, J., Babic, R., Mancilla, H., Licheva, M., Tascher, G., Munch, C., et al. (2023). ULK1-mediated phosphorylation regulates the conserved role of YKT6 in autophagy. J. Cell Sci. *136*, jcs260546. https://doi.org/10.1242/jcs.260546.
56. Li, T.Y., Sun, Y., Liang, Y., Liu, Q., Shi, Y., Zhang, C.S., Zhang, C., Song, L., Zhang, P., Zhang, X., et al. (2016). ULK1/2 Constitute a Bifurcate Node Controlling Glucose Metabolic Fluxes in Addition to Autophagy. Mol. Cell *62*, 359–370. https://doi.org/10.1016/j.molcel.2016.04.009.
57. Schmitz, K., Cox, J., Esser, L.M., Voss, M., Sander, K., Löffler, A., Hillebrand, F., Erkelenz, S., Schaal, H., Kähne, T., et al. (2021). An essential role of the autophagy activating kinase ULK1 in snRNP biogenesis. Nucleic Acids Res. *49*, 6437–6455. https://doi.org/10.1093/nar/gkab452.
58. Sanchez-Martin, P., Saito, T., and Komatsu, M. (2019). p62/SQSTM1: 'Jack of all trades' in health and cancer. FEBS J. *286*, 8–23. https://doi.org/10.1111/febs.14712.
59. Egan, D.F., Chun, M.G.H., Vamos, M., Zou, H., Rong, J., Miller, C.J., Lou, H.J., Raveendra-Panickar, D., Yang, C.C., Sheffler, D.J., et al. (2015). Small Molecule Inhibition of the Autophagy Kinase ULK1 and Identification of ULK1 Substrates. Mol. Cell *59*, 285–297. https://doi.org/10.1016/j.molcel.2015.05.031.
60. Alsaadi, R.M., Losier, T.T., Tian, W., Jackson, A., Guo, Z., Rubinsztein, D.C., and Russell, R.C. (2019). ULK1-mediated phosphorylation of ATG16L1 promotes xenophagy, but destabilizes the ATG16L1 Crohn's mutant. EMBO Rep. *20*, e46885. https://doi.org/10.15252/embr.201846885.
61. Takayama, S., Xie, Z., and Reed, J.C. (1999). An evolutionarily conserved family of Hsp70/Hsc70 molecular chaperone regulators. J. Biol. Chem. *274*, 781–786. https://doi.org/10.1074/jbc.274.2.781.
62. Yim, W.W.Y., Yamamoto, H., and Mizushima, N. (2022). A pulse-chasable reporter processing assay for mammalian autophagic flux with HaloTag. Elife *11*, e78923. https://doi.org/10.7554/eLife.78923.
63. Graef, M., Friedman, J.R., Graham, C., Babu, M., and Nunnari, J. (2013). ER exit sites are physical and functional core autophagosome biogenesis components. Mol. Biol. Cell *24*, 2918–2931. https://doi.org/10.1091/mbc.E13-07-0381.
64. Tan, D., Cai, Y., Wang, J., Zhang, J., Menon, S., Chou, H.T., Ferro-Novick, S., Reinisch, K.M., and Walz, T. (2013). The EM structure of the TRAPPIII complex leads to the identification of a requirement for COPII vesicles on the macroautophagy pathway. Proc. Natl. Acad. Sci. USA *110*, 19432–19437. https://doi.org/10.1073/pnas.1316356110.
65. Szklarczyk, D., Kirsch, R., Koutrouli, M., Nastou, K., Mehryary, F., Hachilif, R., Gable, A.L., Fang, T., Doncheva, N.T., Pyysalo, S., et al. (2023). The STRING database in 2023: protein-protein association networks and functional enrichment analyses for any sequenced genome of interest. Nucleic Acids Res. *51*, D638–D646. https://doi.org/10.1093/nar/gkac1000.
66. Li, L., Jiao, X., D'Atri, I., Ono, F., Nelson, R., Chan, C.C., Nakaya, N., Ma, Z., Ma, Y., Cai, X., et al. (2018). Mutation in the intracellular chloride channel CLCC1 associated with autosomal recessive retinitis pigmentosa. PLoS Genet. *14*, e1007504. https://doi.org/10.1371/journal.pgen.1007504.
67. Dengjel, J., Hoyer-Hansen, M., Nielsen, M.O., Eisenberg, T., Harder, L.M., Schandorff, S., Farkas, T., Kirkegaard, T., Becker, A.C., Schroeder, S., et al. (2012). Identification of autophagosome-associated proteins and regulators by quantitative proteomic analysis and genetic screens. Mol. Cell. Proteomics *11*, M111.014035. https://doi.org/10.1074/mcp.M111.014035.
68. Petherick, K.J., Conway, O.J.L., Mpamhanga, C., Osborne, S.A., Kamal, A., Saxty, B., and Ganley, I.G. (2015). Pharmacological inhibition of ULK1 kinase blocks mammalian target of rapamycin (mTOR)-dependent autophagy. J. Biol. Chem. *290*, 11376–11383. https://doi.org/10.1074/jbc.C114.627778.
69. Cianfanelli, V., De Zio, D., Di Bartolomeo, S., Nazio, F., Strappazzon, F., and Cecconi, F. (2015). Ambra1 at a glance. J. Cell Sci. *128*, 2003–2008. https://doi.org/10.1242/jcs.168153.
70. Carrettiero, D.C., Almeida, M.C., Longhini, A.P., Rauch, J.N., Han, D., Zhang, X., Najafi, S., Gestwicki, J.E., and Kosik, K.S. (2022). Stress routes clients to the proteasome via a BAG2 ubiquitin-independent degradation condensate. Nat. Commun. *13*, 3074. https://doi.org/10.1038/s41467-022-30751-4.
71. Di Bartolomeo, S., Corazzari, M., Nazio, F., Oliverio, S., Lisi, G., Antonioli, M., Pagliarini, V., Matteoni, S., Fuoco, C., Giunta, L., et al. (2010). The dynamic interaction of AMBRA1 with the dynein motor complex regulates mammalian autophagy. J. Cell Biol. *191*, 155–168. https://doi.org/10.1083/jcb.201002100.
72. Dooley, H.C., Razi, M., Polson, H.E.J., Girardin, S.E., Wilson, M.I., and Tooze, S.A. (2014). WIPI2 links LC3 conjugation with PI3P, autophagosome formation, and pathogen clearance by recruiting Atg12-5-16L1. Mol. Cell *55*, 238–252. https://doi.org/10.1016/j.molcel.2014.05.021.
73. Polson, H.E.J., de Lartigue, J., Rigden, D.J., Reedijk, M., Urbé, S., Clague, M.J., and Tooze, S.A. (2010). Mammalian Atg18 (WIPI2) localizes to omegasome-anchored phagophores and positively regulates LC3 lipidation. Autophagy *6*, 506–522. https://doi.org/10.4161/auto.6.4.11863.
74. Axe, E.L., Walker, S.A., Manifava, M., Chandra, P., Roderick, H.L., Habermann, A., Griffiths, G., and Ktistakis, N.T. (2008). Autophagosome formation from membrane compartments enriched in phosphatidylinositol 3-phosphate and dynamically connected to the endoplasmic reticulum. J. Cell Biol. *182*, 685–701. https://doi.org/10.1083/jcb.200803137.
75. Hu, Z., Raucci, S., Jaquenoud, M., Hatakeyama, R., Stumpe, M., Rohr, R., Reggiori, F., De Virgilio, C., and Dengjel, J. (2019). Multilayered Control of Protein Turnover by TORC1 and Atg1. Cell Rep. *28*, 3486–3496.e6. https://doi.org/10.1016/j.celrep.2019.08.069.
76. Loffler, A.S., Alers, S., Dieterle, A.M., Keppeler, H., Franz-Wachtel, M., Kundu, M., Campbell, D.G., Wesselborg, S., Alessi, D.R., and Stork, B. (2011). Ulk1-mediated phosphorylation of AMPK constitutes a negative regulatory feedback loop. Autophagy *7*, 696–706. https://doi.org/10.4161/auto.7.7.15451.
77. Whitmarsh-Everiss, T., and Laraia, L. (2021). Small molecule probes for targeting autophagy. Nat. Chem. Biol. *17*, 653–664. https://doi.org/10.1038/s41589-021-00768-9.
78. Karanasios, E., Stapleton, E., Manifava, M., Kaizuka, T., Mizushima, N., Walker, S.A., and Ktistakis, N.T. (2013). Dynamic association of the ULK1 complex with omegasomes during autophagy induction. J. Cell Sci. *126*, 5224–5238. https://doi.org/10.1242/jcs.132415.
79. Banerjee, C., Mehra, D., Song, D., Mancebo, A., Park, J.M., Kim, D.H., and Puchner, E.M. (2023). ULK1 forms distinct oligomeric states and nanoscopic structures during autophagy initiation. Sci. Adv. *9*, eadh4094. https://doi.org/10.1126/sciadv.adh4094.

80. Nair, U., and Klionsky, D.J. (2005). Molecular Mechanisms and Regulation of Specific and Nonspecific Autophagy Pathways in Yeast. J. Biol. Chem. *280*, 41785–41788. https://doi.org/10.1074/jbc.R500016200.

81. Zaffagnini, G., and Martens, S. (2016). Mechanisms of Selective Autophagy. J. Mol. Biol. *428*, 1714–1724. https://doi.org/10.1016/j.jmb.2016.02.004.

82. Kirkin, V., and Rogov, V.V. (2019). A Diversity of Selective Autophagy Receptors Determines the Specificity of the Autophagy Pathway. Mol. Cell *76*, 268–285. https://doi.org/10.1016/j.molcel.2019.09.005.

83. Kallergi, E., Siva Sankar, D., Matera, A., Kolaxi, A., Paolicelli, R.C., Dengjel, J., and Nikoletopoulou, V. (2023). Profiling of purified autophagic vesicle degradome in the maturing and aging brain. Neuron *111*, 2329–2347.e7. https://doi.org/10.1016/j.neuron.2023.05.011.

84. Owen, D.J., Collins, B.M., and Evans, P.R. (2004). Adaptors for clathrin coats: structure and function. Annu. Rev. Cell Dev. Biol. *20*, 153–191. https://doi.org/10.1146/annurev.cellbio.20.010403.104543.

85. Nalbach, K., Schifferer, M., Bhattacharya, D., Ho-Xuan, H., Tseng, W.C., Williams, L.A., Stolz, A., Lichtenthaler, S.F., Elazar, Z., and Behrends, C. (2023). Spatial proteomics reveals secretory pathway disturbances caused by neuropathy-associated TECPR2. Nat. Commun. *14*, 870. https://doi.org/10.1038/s41467-023-36553-6.

86. Yang, Y., Zheng, L., Zheng, X., and Ge, L. (2021). Autophagosomal Membrane Origin and Formation. Adv. Exp. Med. Biol. *1208*, 17–42. https://doi.org/10.1007/978-981-16-2830-6_2.

87. Ge, L., Zhang, M., Kenny, S.J., Liu, D., Maeda, M., Saito, K., Mathur, A., Xu, K., and Schekman, R. (2017). Remodeling of ER-exit sites initiates a membrane supply pathway for autophagosome biogenesis. EMBO Rep. *18*, 1586–1603. https://doi.org/10.15252/embr.201744559.

88. Fukuzono, T., Pastuhov, S.I., Fukushima, O., Li, C., Hattori, A., Iemura, S.i., Natsume, T., Shibuya, H., Hanafusa, H., Matsumoto, K., and Hisamoto, N. (2016). Chaperone complex BAG2-HSC70 regulates localization of Caenorhabditis elegans leucine-rich repeat kinase LRK-1 to the Golgi. Gene Cell. *21*, 311–324. https://doi.org/10.1111/gtc.12338.

89. Broadbent, D.G., Barnaba, C., Perez, G.I., and Schmidt, J.C. (2023). Quantitative analysis of autophagy reveals the role of ATG9 and ATG2 in autophagosome formation. J. Cell Biol. *222*, e202210078. https://doi.org/10.1083/jcb.202210078.

90. Cook, A.S.I., and Hurley, J.H. (2023). Toward a standard model for autophagosome biogenesis. J. Cell Biol. *222*, e202304011. https://doi.org/10.1083/jcb.202304011.

91. Olivas, T.J., Wu, Y., Yu, S., Luan, L., Choi, P., Guinn, E.D., Nag, S., De Camilli, P.V., Gupta, K., and Melia, T.J. (2023). ATG9 vesicles comprise the seed membrane of mammalian autophagosomes. J. Cell Biol. *222*, e202208088. https://doi.org/10.1083/jcb.202208088.

92. Jin, J., Arias, E.E., Chen, J., Harper, J.W., and Walter, J.C. (2006). A family of diverse Cul4-Ddb1-interacting proteins includes Cdt2, which is required for S phase destruction of the replication factor Cdt1. Mol. Cell *23*, 709–721. https://doi.org/10.1016/j.molcel.2006.08.010.

93. Antonioli, M., Albiero, F., Nazio, F., Vescovo, T., Perdomo, A.B., Corazzari, M., Marsella, C., Piselli, P., Gretzmeier, C., Dengjel, J., et al. (2014). AMBRA1 Interplay with Cullin E3 Ubiquitin Ligases Regulates Autophagy Dynamics. Dev. Cell *31*, 734–746. https://doi.org/10.1016/j.devcel.2014.11.013.

94. Nazio, F., Strappazzon, F., Antonioli, M., Bielli, P., Cianfanelli, V., Bordi, M., Gretzmeier, C., Dengjel, J., Piacentini, M., Fimia, G.M., and Cecconi, F. (2013). mTOR inhibits autophagy by controlling ULK1 ubiquitylation, self-association and function through AMBRA1 and TRAF6. Nat. Cell Biol. *15*, 406–416. https://doi.org/10.1038/ncb2708.

95. Di Rienzo, M., Antonioli, M., Fusco, C., Liu, Y., Mari, M., Orhon, I., Refolo, G., Germani, F., Corazzari, M., Romagnoli, A., et al. (2019). Autophagy induction in atrophic muscle cells requires ULK1 activation by TRIM32 through unanchored K63-linked polyubiquitin chains. Sci. Adv. *5*, eaau8857. https://doi.org/10.1126/sciadv.aau8857.

96. Cox, J., and Mann, M. (2008). MaxQuant enables high peptide identification rates, individualized p.p.b.-range mass accuracies and proteome-wide protein quantification. Nat. Biotechnol. *26*, 1367–1372. https://doi.org/10.1038/nbt.1511.

97. Shannon, P., Markiel, A., Ozier, O., Baliga, N.S., Wang, J.T., Ramage, D., Amin, N., Schwikowski, B., and Ideker, T. (2003). Cytoscape: a software environment for integrated models of biomolecular interaction networks. Genome Res. *13*, 2498–2504. https://doi.org/10.1101/gr.1239303.

98. Bindea, G., Mlecnik, B., Hackl, H., Charoentong, P., Tosolini, M., Kirilovsky, A., Fridman, W.H., Pagès, F., Trajanoski, Z., and Galon, J. (2009). ClueGO: a Cytoscape plug-in to decipher functionally grouped gene ontology and pathway annotation networks. Bioinformatics *25*, 1091–1093. https://doi.org/10.1093/bioinformatics/btp101.

99. Kaeser-Pebernard, S., Vionnet, C., Mari, M., Sankar, D.S., Hu, Z., Roubaty, C., Martínez-Martínez, E., Zhao, H., Spuch-Calvar, M., Petri-Fink, A., et al. (2022). mTORC1 controls Golgi architecture and vesicle secretion by phosphorylation of SCYL1. Nat. Commun. *13*, 4685. https://doi.org/10.1038/s41467-022-32487-7.

100. Labun, K., Montague, T.G., Krause, M., Torres Cleuren, Y.N., Tjeldnes, H., and Valen, E. (2019). CHOPCHOP v3: expanding the CRISPR web toolbox beyond genome editing. Nucleic Acids Res. *47*, W171–W174. https://doi.org/10.1093/nar/gkz365.

101. Wiśniewski, J.R., Zougman, A., Nagaraj, N., and Mann, M. (2009). Universal sample preparation method for proteome analysis. Nat. Methods *6*, 359–362. https://doi.org/10.1038/nmeth.1322.

102. Tyanova, S., Temu, T., and Cox, J. (2016). The MaxQuant computational platform for mass spectrometry-based shotgun proteomics. Nat. Protoc. *11*, 2301–2319. https://doi.org/10.1038/nprot.2016.136.

103. Perez-Riverol, Y., Bai, J., Bandla, C., García-Seisdedos, D., Hewapathirana, S., Kamatchinathan, S., Kundu, D.J., Prakash, A., Frericks-Zipper, A., Eisenacher, M., et al. (2022). The PRIDE database resources in 2022: a hub for mass spectrometry-based proteomics evidences. Nucleic Acids Res. *50*, D543–D552. https://doi.org/10.1093/nar/gkab1038.

104. James, P., Halladay, J., and Craig, E.A. (1996). Genomic libraries and a host strain designed for highly efficient two-hybrid selection in yeast. Genetics *144*, 1425–1436. https://doi.org/10.1093/genetics/144.4.1425.

STAR★METHODS

KEY RESOURCES TABLE

REAGENT or RESOURCE	SOURCE	IDENTIFIER
Antibodies		
Mouse monoclonal, Anti-β-Actin	Santa Cruz Biotechnologies	Cat#sc-47778; RRID:AB_626632
Rabbit polyclonal, SQSTM1/P62	Cell Signaling	Cat#5114S; RRID:AB_10624872
Rabbit, polyclonal LC3A/B	Cell Signaling	Cat#4108S; RRID:AB_2137703
Mouse, monoclonal LC3B	Nanotoold	Cat# 0231-100/LC3-5F10; RRID:AB_2722733
Rabbit monoclonal, ATG14	Cell Signaling	Cat#96752; RRID:AB_2737056
Rabbit monoclonal, ATG14, p29	Cell Signaling	Cat#92340S; RRID:AB_2800182
Rabbit monoclonal, FIP200	Cell Signaling	Cat#12436S; RRID:AB_2797913
Rabbit monoclonal, ULK1	Cell Signaling	Cat#8054; RRID:AB_11178668
Rabbit polyclonal, ULK1, p757	Cell Signaling	Cat#6888S; RRID:AB_10829226
Rabbit polyclonal, ATG13	Sigma	Cat# SAB4200100; RRID:AB_10602787
Rabbit polyclonal, ATG101	Cell Signaling	Cat#13492; RRID:AB_2798234
Mouse monoclonal, BAG2	Santa Cruz Biotechnologies	Cat#sc-390107; RRID:AB_2936954
Mouse monoclonal, BAG3	Santa Cruz Biotechnologies	Cat#sc-136467; RRID:AB_10647772
Mouse monoclonal, BAG5	Santa Cruz Biotechnologies	Cat#sc-390832; RRID:AB_2936955
Rabbit polyclonal, CLCC1	Atlas	Cat#HPA013210; RRID:AB_1846895
Mouse monoclonal, WIPI2	BioRad	Cat#MCA5780GA; RRID:AB_10845951
Mouse monoclonal, AMBRA1	Santa Cruz Biotechnologies	Cat#sc-398204; RRID:AB_2861324
Rabbit monoclonal, RAB7	Abcam	Cat#ab137029; RRID:AB_2629474
Mouse monoclonal, Halo-Tag	Promega	Cat#G9211; RRID:AB_2688011
Mouse monoclonal, HSP90	Santa Cruz Biotechnologies	Cat#sc-13119; RRID:AB_675659
Peroxidase conjugated anti-mouse monoclonal IgG	Jackson Immuno research	Cat#111-035-062; RRID: AB_2338504
Peroxidase conjugated anti-rabbit monoclonal IgG	Jackson Immuno research	Cat#111-035-045; RRID: AB_2337938
Mouse monoclonal, BAG2	Novus Biologicals	Cat#NBP2-59476
Mouse monoclonal, ERGIC	Enzo	Cat#ENZ-ABS300-0100
Mouse monoclonal, SNX1	BD Biosciences	Cat#611482; RRID:AB_398942
Donkey anti-mouse IgG (H + L) Alexa Fluor 488	ThermoFisher	Cat#A21202; RRID:AB_141607
Rabbit polyclonal, AMBRA1	Millipore	Cat#ABC131; RRID:AB_2636939
Goat anti-rabbit Alexa Fluor 633	ThermoFisher	Cat#A21071; RRID:AB_2535732
Bacterial and virus strains		
E. coli DH5α	CGSC	Cat#12384
Chemicals, peptides, and recombinant proteins		
DMEM	PAN Biotech	Cat#P04-04510
SILAC-DMEM	PAN Biotech	Cat#P04-02505
DPBS	PAN Biotech	Cat#P04-36500
HBSS	Gibco	Cat#14025100
FBS	Biowest	Cat#S181B-500
Dialyzed FBS	Biowest	Cat#S181D-500
Penicillin/streptomycin	PAN Biotech	Cat#P06-07100
GlutaMAX	GIBCO	Cat# 3505003
Trypsin for cell culture	PAN Biotech	Cat#P10-023100
Pierce Anti-HA Magnetic Beads	ThermoFisher	Cat#13474229
Strep-Tactin®XT 4Flow®	IBA	Cat#2-5030-010
Nitrocellulose membrane 0.45 μm	Amersham	Cat#GE10600000

(*Continued on next page*)

Continued

REAGENT or RESOURCE	SOURCE	IDENTIFIER
PVDF membrane 0.2 μm	Amersham	Cat#GE10600021
TransBlot Turbo RTA Midi NC	Bio-Rad	Cat#1704271
TransBlot Turbo RTA Midi PVDF	Bio-Rad	Cat#1704273
WesternBright ECL	Advansta	Cat#K12049-D50
Benzonase	Sigma-Aldrich	Cat#1.01697.0001
Arg10	Sigma-Aldrich	Cat#608033
Arg6	Sigma-Aldrich	Cat#643440
Lys4	Sigma-Aldrich	Cat#616192
Lys8	Sigma-Aldrich	Cat#608041
Arg0	Sigma-Aldrich	Cat#11039
Lys0	Sigma-Aldrich	Cat#L8662
L-Proline	Fluka	Cat#81710
PhosSTOP	Roche	Cat#04-906-837-001
Proteases Inhibitor Cocktail	Roche	Cat#11-697-498-001
Bafilomycin A1	Santa Cruz Biotechnologies	Cat#sc-201550A
Concanamycin A (conA)	Sigma-Aldrich	Cat#C9705
MRT68921	Merck	Cat#SML1644
Trifluoroacetic acid (TFA)	Sigma-Aldrich	Cat#302031
Formic acid (FA)	Merck	Cat#5.43804.0250
Ammonia solution 25%	Merck	Cat#5438300250
Trypsin	Promega	Cat#V5113
ATP	Sigma-Aldrich	Cat#A6419
Vivacon 500, 10′000 MWCO HYDROSART	Sartorius	Cat#VN01H02
cDNA	Qiagen QuantiTect RT-PCR kit	Cat#205311
C18 disc	3M Empore	Cat#14-386-2
MS-grade Water	VWR	Cat#23595.328
MS-grade Acetonitrile	VWR	Cat#20060.320
Bio-Rad Protein Assay Dye Reagent Concentrate	Bio-Rad	Cat#5000-0006
Biotin	Sigma-Aldrich	Cat#B4501
Puromycin	Invivogen	Cat#ant-pr-1
Blasticidin	Invivogen	Cat#ant-bl-1
Hygromycin	Invivogen	Cat#ant-hg-1
collagen I	ThermoFisher	Cat#A10483-01
horse serum	ThermoFisher	Cat#16050
Hoechst 33342 solution	Sigma-Aldrich	Cat#14533
ProLong Gold antifade reagent	ThermoFisher	Cat#P36931
TG buffer	VWR	Cat#0307
High-capacity binding streptavidin beads	ThermoFisher	Cat#20361
TMR ligand	Promega	Cat#G8251
Lambda Protein Phosphatase	NEB	Cat#P0753L
Polybrene	Sigma-Aldrich	Cat#H9268
Lipofectamine LTX reagent	ThermoFisher	Cat#15338030
Critical commercial assays		
Pierce^{TM} BCA Protein Assay Kit	Thermo Scientific	Cat#23225
WesternBright ECL	Advansta	Cat#K12049-D50
SuperSignal West Femto Chemiluminescent	Thermo Scientific	Cat#PIER34096
Deposited data		
Western blot uncropped images	Mendeley Data	https://doi.org/10.17632/24jp9dk4gj.1
Proteomics raw data files	ProteomeXchange	PXD044974

(*Continued on next page*)

Continued

REAGENT or RESOURCE	SOURCE	IDENTIFIER
Experimental models: cell lines		
HeLa cells	ATCC	CRM-CCI-2
HeLa ULK1 KO, (Figures 1A and 1B)	This study	N/A
HeLa ATG13 KO, (Figures 1A and 1B)	This study	N/A
HeLa ATG101 KO, (Figures 1A and 1B)	This study	N/A
HeLa FIP200 KO, (Figures 1A and 1B)	This study	N/A
HeLa BAG2 KO, (Figures 3D, 3E, 3F, and 3J), Figures 6F and 6G, S4A–S4C, S4F, and S4G), S5A and S5B	This study	N/A
HeLa ULK1 KO, N-HA-MT-ULK1 (Figures 1A–1F, and 2A–2C (Figure S1)	This study	N/A
HeLa ULK1 KO, ULK1-MT-HA-C (Figures 1A–1F, and 2A–C (Figure S1)	This study	N/A
HeLa ULK1 KO, N-HA-MT-GFP (Figures 1A–1F, and 2A–2C (Figure S1)	This study	N/A
HeLa ATG13 KO, N-HA-MT-ATG13 (Figures 1A–1F, and 2A–2C (Figure S1)	This study	N/A
HeLa ATG13 KO, ATG13-MT-HA-C (Figures 1A–1F, and 2A–2C (Figure S1)	This study	N/A
HeLa ATG13 KO, N-HA-MT-GFP (Figures 1A–F, and 2A–2C (Figure S1)	This study	N/A
HeLa ATG101 KO, N-HA-MT-ATG101 (Figures 1A–1F, and 2A–2C) (Figure S1)	This study	N/A
HeLa ATG101 KO, ATG101-MT-HA-C (Figures 1A–1F, and 2A–2C (Figure S1)	This study	N/A
HeLa ATG101 KO, N-HA-MT-GFP (Figures 1A–1F, and 2A–2C (Figure S1)	This study	N/A
HeLa FIP200 KO, N-HA-MT-FIP200 (Figures 1A–1F, and 2A–2C (Figure S1)	This study	N/A
HeLa FIP200 KO, FIP200-MT-HA-C (Figures 1A–1F, and 2A–2C (Figure S1)	This study	N/A
HeLa FIP200 KO, N-HA-MT-GFP (Figures 1A–1F, and 2A–2C (Figure S1)	This study	N/A
HeLa BAG2 KO, SHA-BAG2 (Figures 3B, 3C, 5A, 5B, 5C, 5F, 5G, 6A–6E, 6H, and 6I)	This study	N/A
HeLa BAG2 KO, SHA-BAG2 S31A (Figures 7C, and 7D–7I)	This study	N/A
HeLa BAG2 KO, SHA-BAG2 S31E (Figures 7C, and 7D–7I)	This study	N/A
HeLa BAG2 KO, SHA-BAG2 I160A (Figures 3D and 3E)	This study	N/A
HeLa SHA-ULK1 (Figure 7B)	Hu et al.[54]	N/A
HeLa SHA-ULK1 D165A (Figure 7B)	Hu et al.[54]	N/A
HeLa Halo-LC3, Figures S4D and S4E)	This study	N/A
HeLa ER-GFP, (Figures 6F and 6G)	Di Bartolomeo et al.[71]	N/A
Oligonucleotides		
(full list see Table S5)		N/A
sgRNA/shRNA sequences	Oligonucleotide number	Target gene
GCTACGAGAAGAACAAGACGT	CRONDS1	ULK1_1
GCAGGTTTCGCTCAATGCGC	CRONDS2	ULK1_2
ACTTGGCATTCATGTCTACCA	CRONDS3	ATG13_1
TCTTGAGAGTCTTCTACAGAC	CRONDS4	ATG13_2
GTAGTTTTAGGAATAGCAGG	CRONDS6	FIP200
ACCAGAAGAAGAAGTCTCGCTGG	CRONDS7	ATG101_1

(*Continued on next page*)

Continued

REAGENT or RESOURCE	SOURCE	IDENTIFIER
GTTATCCACCTCCGACTGTGTGG	CRONDS8	ATG101_2
GATCAACGCTAAAGCCAACGAGG	CRONDS9	BAG2_1
CACCTCATCAATAATCCTTGTGG	CRONDS10	BAG2_2
CCGGGATCAGAAGTTTCAATCCATACTCG AGTATGGATTGAAACTTCTGATCTTTTTG	TRC0000033591	shRNA-1 (BAG2)
Recombinant DNA		
BAG2 cDNA	This study	N/A
ATG101 cDNA	This study	N/A
ULK1	Hu et al.[54]	N/A
ULK1 D165A	Hu et al.[54]	N/A
ATG13	Gift from Dr. Björn Stork	N/A
FIP200	Gift from Dr. Björn Stork	N/A
miniTurbo	Addgene	107172
pLK01_shRNABAG, TRC0000033591	NEXUS Personalized Health Technologies	N/A
Halo tag	DNASU	HsCD00840399
Modified pCW57.1, SV40-Puromycin was replaced with MND-Blasticidin	Hu et al.[54]	N/A
ULK1 CRISPR plasmid	This study	N/A
ATG13 CRISPR plasmid	This study	N/A
ATG101 CRISPR plasmid	This study	N/A
FIP200 CRISPR plasmid	This study	N/A
BAG2 CRISPR plasmid	This study	N/A
Rat LC3B (rLC3B)	IDTDNA	N/A
Software and algorithms		
ImageJ	NIH	https://imagej.nih.gov/ij/index.html,
Photoshop, v.22.5.1	Adobe	https://www.adobe.com/
MaxQuant	Cox and Mann[96]	https://maxquant.net/maxquant/
Perseus	Cox and Mann[96]	https://maxquant.net/perseus/
Cytoscape	Shannon et al., 2003[97]	https://cytoscape.org/
ClueGO	Bindea et al., 2009[98]	http://apps.cytoscape.org/apps/cluego
Imaris v.10.0.0	Bitplane, Oxford Instruments	https://imaris.oxinst.com/

EXPERIMENTAL MODEL AND STUDY PARTICIPANT DETAILS

HeLa cells (ATCC CCl-2) were validated by genotyping (Microsynth) and negatively tested for mycoplasma. All cells were grown in a humidified incubator in Dulbecco's modified Eagle medium (DMEM, PAN Biotech, P04-04510) supplemented with 10% fetal bovine serum (FBS, BioWest, S181B-500), 1% penicillin/streptomycin (PAN Biotech, P06-07100) at 37°C and 5% CO2. For SILAC labeling, cells were cultured for seven generations using SILAC-DMEM, containing non-labeled and labeled lysine and arginine variants: Lys-8 (Sigma, 608041) and Arg-10 (Sigma, 608033) for heavy, Lys-4 (Sigma, 616192) and Arg-6 (Sigma, 643440) for medium, and Lys-0 (Sigma, L8662) and Arg-0 (Sigma, 11039) for light labels, supplemented with 10% dialyzed FBS (Biowest, S181D-500)1% penicillin/streptomycin and 1% glutamax (GIBCO, 35050038). The final concentration of arginine was 42 mg/L, lysine of 73 mg/L and to avoid the conversion of arginine to proline, L-proline 26 mg/L was added. For phenotype assays, HA affinity purification, and cellular fractionation experiments, starvation was induced by incubating cells with Hank's Balanced Salt solution (HBSS, ThermoFisher, 14025-100) for 2 h. For proximity labeling experiments and HA affinity purification of ULK1 complex members, cells were incubated with HBSS for 90 min. In all indicated experiments 10 nM concanamycin A (Sigma-Aldrich, C9705) or 2 nM Bafilomycin A1 (Santa Cruz Biotechnologies, sc-201550A) were used. ER-GFP stably expressing HeLa cells were obtained by culturing pCMV/Myc/ER-GFP–transfected cells in the presence of 0.4 mg/mL G418 (ThermoFisher) for 2 weeks.[71]

METHOD DETAILS

Cloning of recombinant DNA constructs

The following gene-encoding plasmids were generous gifts from Prof Björn Stork: ULK1 WT, ULK1 KD (kinase dead, D165A), ATG13 isoform II, and FIP200/RB1CC1. BAG2 and ATG101 were amplified by RT-PCR from HEK293T cDNA (Qiagen QuantiTect RT-PCR kit, 205311) using primers oNDS227 and oNDS228 for ATG101, and oNDS309 and oNDS310 for BAG2 (please see Table S2A for all primer sequences). The GFP gene was PCR amplified using primers oNDS139 and oNDS140 from pEGFP-C1-puromycin plasmid to make the miniTurbo-GFP fusion (pDS48) plasmid. miniTurbo containing plasmid 3xHA-miniTurbo-NLS_pCDNA3 was a gift from Alice Ting (Addgene plasmid # 107172). miniTurbo gene (primers: oNDS:115 and 116) was fused N-terminal to all constructs (ULK1 (pDS38) (oNDS:117 and 118), FIP200 (pDS41) (oNDS:121 and 122), ATG13 (pDS40) (oNDS:119 and 120) and ATG101 (pDS42) (oNDS:231 and 232)) starting with N-terminal HA-tag, miniTurbo, V5-tag and the gene of interest. Similarly, for the C-terminal tagging, the sequence starts with N-terminal gene constructs (ULK1 (pDS43) (oNDS:190 and 191), FIP200 (pDS46) (oNDS:188 and 189), ATG13 (pDS45) (oNDS:225 and 226) and ATG101 (pDS47) (oNDS:229 and 230)), followed by V5-tag, miniTurbo (oNDS:132 and 133) and HA tag at the C-terminal end. A PCR fragment of miniTurbo containing HA- and V5-tag was generated and another PCR product for gene of interest (please see Table S1A for primer sequences) having the V5-tag and homology arms with the vector was generated. All PCR reactions were performed using the Phusion high fidelity DNA polymerase (NEB, M0530S). All the PCR-amplified fusion genes and epitope tags were cloned into the pSKP32 vector[99] between the NheI and PstI restriction sites using Gibson assembly (NEB, M5510A) according to manufacturer's protocol. Using the same method, HA-2X-Streptactin tag (SHA, (primers: oNDS107/111)) was fused to the N-terminal of BAG2 WT (pDS49) (primers: oNDS318/319), phospho-mutants (BAG2-S31A (pDS50) (primers: oNDS345/348/346/347), and S31E (pDS51) (primers: oNDS345/348/349/350) genes and cloned into pSKP32. HSC/HSP70 deficient mutant BAG2 I160A (pDS52) (primers: oNDS345/348/379/380) was also cloned the same way in pSKP32. The pSKP32 vector was used as a negative/beads control for all SHA experiments. A pSKP190 destination vector was generated by replacing the hPGK-Puromycin resistance cassette of pCW57.1 (gift from David Root (Addgene plasmid # 41393; http://n2t.net/addgene:41393; RRID:Addgene_41393)) between the AgeI/XbaI restriction sites with a mPGK-Hygromycin resistance cassette PCR amplified from pER81 (generous gift from Richard Iggo) using oSKP-286/287 by Gibson assembly. The inducible Halo-rLC3B expression lentiviral vector pSKP199 was generated as follows. The Halo tag gene was purchased from DNASU (HsCD00840399), PCR amplified (primers: oSKP 298/299), andprecombinant rat LC3B (rLC3B) was synthesized as a double stranded gene block (IDTDNA). pSKP190 was double digested with NdeI/BsrGI. Gibson assembly was performed by assembling Halo tag, rLC3B (for sequence please see S2F) and the double digested pSKP190 vector. All the cloning constructs were sequence confirmed (Eurofins) with the listed primers (please see Table S2B for primer sequences).

Cloning of CRISPR Cas-9 knockout vectors and cell line generation

CRISPR knockouts of BAG2, ULK1, FIP200, ATG13 and ATG101 in HeLa cells were performed using sgRNAs (single guide RNAs, please see Table S2C for guide RNA sequences) cloned in pX330-U6-Chimeric_BB-CBh-hSpCas9 (gift from Feng Zhang (Addgene plasmid # 42230; http://n2t.net/addgene:42230; RRID:Addgene_42230)). The sgRNAs were designed using CHOPCHOP CRISPR guide RNA algorithm,[100] CRISPR plasmids and pEGFP-C1 puromycin plasmids were co-transfected in HeLa cells using lipofectamine LTX reagent (ThermoFisher, 15338030), according to manufacturer's instructions. 24h post-transfection, co-transfected cells were selected in culture medium supplemented with 3 mg/mL puromycin (Invivogen, ant-pr-1), until selection was complete after about 48 h. Efficiently transfected cells were isolated to generate clonal lineages by single-cell cloning in 96-well plates; colonies were all evaluated for KO efficiency by western blot against the targeted protein. shRNAs were obtained from NEXUS Personalized Health Technologies (ETH Zürich). Scrambled shRNA as a control and shRNABAG2 (TRC0000033591, for sequence see above) chosen from the Broad RNAi consortium were used for knockdown experiments. The above sequences were cloned between AgeI and EcoRI sites in pLKO.1 vector containing puromycin resistance gene leading to constitutive expressing. All cloning constructs were sequence confirmed using primer oNDS317.

Lentivirus production and infection of target cells

To produce replication-defective lentiviral particles, recombinant DNA constructs cloned in lentiviral plasmids described above were co-transfected with packaging and envelope plasmids psPAX2 (gift from Didier Trono (Addgene plasmid # 12260; http://n2t.net/addgene:12260; RRID:Addgene_12260)) and pMD2.G (gift from Didier Trono (Addgene plasmid # 12259; http://n2t.net/addgene:12259; RRID:Addgene_12259)) into HEK293T cells seeded the night before using JetPrime transfection reagent (Polyplus, 114-75). Transfection medium was changed 12 h post transfection, and lentiviral supernatants were harvested 24 h later, sterile filtered through 0.2 μm syringe filters, supplemented with 8 μg/mL polybrene (Sigma-Aldrich, H9268), and stored in aliquots at −80°C. Lentiviral particles having different miniTurbo fusion constructs were used to infect respective HeLa ULK1 KO, ATG13 KO, FIP200 KO, and ATG101 KO cells. SHA-BAG2, BAG2 phospho-variants and corresponding vector control viral particles were used to infect the indicated BAG2 KO clones. Halo-rLC3B tag lentiviral particles were used to infect HeLa WT and BAG2 KO clones. To infect, viral dilutions (1:2 to 1:1000) were used in DMEM supplemented with 8 μg/mL polybrene. Infected cells were selected 24 h post infection in 4 μg/mL Blasticidin (Invivogen, ant-bl-1) or 100 μg/mL of hygromycin (Invivogen, ant-hg-1), according to the respective lentiviral selection marker, until selection was complete. Selected cells were tested for ectopic expression using doxycycline

(2 mg/mL) inducible promoters by western blotting against the respective proteins-of-interest using anti-HA antibodies to determine the best working dilution. For knockdown experiments, shRNA-expressing lentiviruses were generated and used to infect the indicated target cells with the same protocol. 24 h post-infection, cells were selected in culture medium supplemented with 3 μg/mL puromycin (Invivogen, ant-pr-1), and selection was completed for 48 h before cells were harvested. Western blot analysis against BAG2 protein was performed using cell lysates to check efficiencies of shRNAs and the best shRNA was chosen for all shRNA related experiments. For shRNA experiments in Halo-rLC3B-expressing cells, a similar protocol was applied to the exception of Halo-rLC3B induction that was performed 24 h before TMR pulsing and harvesting.

Antibodies

For western blotting experiments, all primary antibodies were used at a concentration of 1:1000 in either 5% milk or 5% BSA in 1X TBST buffer (1X TBS (Tris-buffered saline), 0.1% Tween 20). Secondary antibodies were used at dilutions of 1:10′000 for anti-rabbit and 1:5′000 for anti-mouse in 5% milk or 5% BSA in 1X TBST. All primary and secondary antibodies were tested according to the manufacturer's protocols. The following primary antibodies were used: Anti-β-Actin, SQSTM1/P62, LC3A/B, ATG14, ATG14-p29, FIP200, ULK1, ULK1-p757, ATG13, ATG101, BAG2, BAG3, BAG5, CLCC1, WIPI2, AMBRA1, RAB7, Halo-Tag, and HSP90. Secondary antibodies used in the western blots were: Peroxidase conjugated anti-mouse monoclonal IgG (Jackson Immuno research, 111-035-062, RRID: AB_2338504), Peroxidase conjugated anti-rabbit monoclonal IgG (Jackson Immuno research, 111-035-045, RRID: AB_2337938).

For immunofluorescence (IF) experiments, all primary antibodies were used at a 1:100 dilution. In addition to those mentioned above, the following primary antibodies were used only in IF experiments: BAG2 (Novus Biologicals, NBP2-59476, mouse), ERGIC53 (Enzo, ENZ-ABS300-0100, mouse), SNX1 (BD Biosciences, 611482, mouse). Secondary antibodies used for IF were: donkey anti-mouse IgG (H + L) Alexa Fluor 488 (ThermoFisher, A21202), goat anti-rabbit Alexa Fluor 633 (ThermoFisher, A21071).

Immunostainings and florescence microscopy analysis

For immunofluorescence analysis, the indicated cells were seeded on collagen I (ThermoFisher, A10483-01, diluted in 0.02 M acetic acid to 50 mg/mL)-coated coverslips for 24 h prior to experiments. Cells were treated as indicated and further fixed using either ice-cold 100% methanol (MetOH) or PFA (paraformaldehyde) for 15 min. Before and after fixing, the cells were washed 6 times in 1X PBST (1X PBS, 0.1% Tween 20), and only following PFA fixation, cells were permeabilized with 0.1% Triton X-100. After fixing, cells were blocked in 1X PBST containing 5% horse serum (ThermoFisher, 16050) for 30 min, and finally washed 6 times in 1X PBST. Cells were incubated in a wet chamber with a primary antibody solution 1:100 diluted in 5% horse serum in 1X PBST, overnight at 4°C. Cells were then washed 6 times in 1X PBST and incubated in the secondary antibody solution with dilution 1:2000 in the dark, for 2 h at room temperature. After incubation, cells were washed 6 times with 1X PBST, incubated in 10 μM Hoechst 33342 solution (Sigma-Aldrich, 14533) for 1 min, washed again 6 times, and embedded in ProLong Gold antifade reagent (ThermoFisher, P36931). Confocal imaging was performed using a Leica STELLARIS 8 FALCON system. Images were analyzed, quantified, and prepared with Fiji (v.2.3.0) and Imaris (v.10.0.0, Bitplane, Oxford Instruments), employing intensity thresholding, size exclusion, and noise filtering, based on signal intensities of the control. P62/SQSTM1 and WIPI2 foci were detected using the Spots tool based on the most intense fluorescent regions (growing spots with a minimal radius of 0.2 μm, no vertical correction applied). Abnormal or dead cells were manually excluded. Nuclei were detected using the Surface tool, and nuclei close to the edges were excluded. p62/SQSTM1 and WIPI2 foci belonging to excluded cells were then manually excluded before automated counting was applied. A minimum of 100 cells were analyzed per condition and replicate. Spots and surfaces were detected automatically ("per batch") using the same parameters throughout each experiment to avoid any user-induced bias.

BAG2 and CLCC1 colocalization was determined using the Imaris Coloc extension for intensity-based colocalization (Imaris v.10.0.0, Bitplane, Oxford Instruments). 20 cells were analyzed per condition and biological replicated. To address the nested structure of data, i.e., day of the observation and the number cells, significance was determined with a two-way ANOVA using the condition and the replicate as factors following a TukeyHSD post-hoc test to identify significant differences between two conditions. Single cell images were generated using Fiji (v.2.9.0) and Adobe Photoshop (v.22.5.1) softwares. Background subtraction, Gaussian filter and brightness/contrast adjustment were applied identically to each picture displayed on a same panel. To determine ER localization of AMBRA1, ER-GFP expressing HeLa cells were examined with an LSM 900, Airyscan SR Zeiss confocal microscopy. A minimum of 25 cells/sample was analyzed and the statistical analysis was performed using ANOVA 2-way test for repeated samples by using Graphpad Prism, p values of less than 0.05 were considered significant.

Cell lysis

For immunoblotting analyses of whole cell lysates and Halo-LC3 tag assays, cells from 1 × 10 cm dish were lysed in modified RIPA with SDS (50 mM Tris, 150 mM NaCl, 2% SDS, 0.5% sodium deoxycholate, 1% Triton X-100, EDTA-free 1x protease inhibitors (Roche, 11-697-498-001), 1x PhosSTOP (Roche, 04-906-837-001, 1:5000 Benzonase), pH-7.5). For HA-based affinity purifications of ULK1 complex members (ULK1, ATG101, ATG13 and FIP200), SILAC labeled cells of 2 × 15 cm dishes for each label were lysed in normal lysis buffer (50 mM Tris, 150mM NaCl, 1 mM EDTA, 0.1% SDS, 0.5% sodium deoxycholate, 1% Triton X-100, EDTA-free 1x protease inhibitors (Roche, 11-697-498-001), pH-7.5). For HA-based affinity purifications of SHA-BAG2 WT and phospho-variants, 2 × 15 cm dish of cells per replicate were lysed in BAG2 IP buffer (50 mM Tris, 150 mM NaCl, 1 mM EDTA, 1 mM EGTA, 0.35% Triton

X-100, EDTA-free 1x protease inhibitors (Roche, 11-697-498-001), pH-7.5). Similar lysis buffer conditions were used for HA-based affinity purification of SHA-BAG2 in presence and absence with 20 mM of the ULK1 inhibitor MRT68921 (Merck, SML1644) (2 h prior HBSS treatment, total of 4 h). For endogenous AMBRA1 immunoaffinity purifications (antibody ABC131, Millipore), 2 × 15 cm dishes of cells per replicate were lysed in AMBRA1 IP buffer (10 mM Tris, 150 mM NaCl, 10% glycerol, 0.5% NP-40, EDTA-free 1x protease inhibitors (Roche, 11-697-498-001), pH-8). All cell lysates were vortexed 4 times for 15 s, and lysis was done for 30 min on ice. Lysates were centrifuged at 14000 rpm for 10 min at 4°C. Protein quantification was determined by BCA assay as per manufacturer's protocol (ThermoFisher, 23225). Proteins concentrations were adjusted with corresponding lysis buffers to yield equal protein amounts per lane in all respective experiments.

Immunoblotting

Cell extracts were denatured in 1X Laemmli buffer (62.5 mM Tris pH 6.8, 2% SDS, 10% glycerol, 0.1 M DTT, 0.01% bromophenol blue), vortexed for 4 s and heated at 75°C for 10min. For western blotting, 30 μg of total protein were loaded per well and separated by SDS-PAGE. Proteins were transferred to a 0.45 μm nitrocellulose membrane for proteins larger than 35 kDa and to 0.1 μm nitrocellulose or 0.2 μm PVDF membranes for proteins smaller than 35 kDa for 30 min using Trans-Blot Turbo transfer system (Bio-Rad, 1704150) or for 2.5 h using wet transfer system (TG buffer, VWR, 0307) under a constant electric current. Membranes were blocked for minimum 1 h in either 5% milk or 5% BSA in 1xTBST (10 mM Tris, 150 mM NaCl and 0.1% Tween 20). Membranes were incubated with the indicated primary antibodies overnight on a shaker at 4°C. Membranes were washed with 1x TBST four times 10 min and incubated with the appropriate peroxidase-conjugated secondary antibodies in 5% milk or 5% BSA in 1xTBST for 1 h at RT. Membranes were washed with 1xTBST four times 15 min. Blotted proteins were visualized using either SuperSignal West Femto chemiluminescent (ThermoFischer, PIER34096) or WesternBright ECL-(Advansta, K-12045-D50) reagents. Images were recorded with the Odyssey Fc reader (LI-COR Biosciences-GmbH, Image Studio v.2.0.38) and densitometry analyses were performed using ImageJ Fiji software (Wayne Rasband, NIH).

Whole proteome analyses

For whole proteome analyses of HeLa WT and HeLa KO cells (BAG2, ULK1, FIP200, ATG13, ATG101), 1 × 10 cm dish for each replicate per condition was lysed in 1% sodium deoxycholate, 50 mM Tris buffer, at pH = 8. Samples were incubated with 1 mM DTT, heated for 10 min at 75°C followed by 5.5 mM IAA incubated for 10 min in dark at RT. Trypsin was added with 1:100 ratio (Trypsin: protein, w/w) and samples were left for digestion overnight at 37°C. TFA was added drop-wise to completely precipitate sodium deoxycholate and centrifuged at 14000 rpm, 23°C. Supernatants containing the peptides were STAGE tip-purified and dissolved in buffer A (0.1% formic acid in MS grade water) for LC-MS/MS measurements.

Cell fractionation

Cells of 2 × 15 cm dishes for each cell line per replicate were cultured 36 h prior to indicated treatments and culture medium was changed 16 h before the treatments. Cell pellets were dissolved in homogenization (HM) buffer (0.25 M Sucrose, 1 mM EDTA, 20 mM HEPES-NaOH pH 7.4), supplemented with EDTA-free 1x protease inhibitors (Roche, 11-697-498-001). The cells were taken up in HM buffer and dounced 550 times followed by several centrifugation steps of supernatants from the preceding fractions to collect nuclear (1′000 g, 15 min, 4°C), mitochondria (3′000 g, 15 min, 4°C), and vesicular fractions (17′000 g, 15 min, 4°C). The last supernatant was collected as the cytosolic fraction. 1% of whole cell lysates were taken from respective samples prior fractionations. All pellets of individual fractions were washed twice with HM buffer. The pellets from mitochondria and vesicular fractions were resuspended in RIPA buffer (50 mM Tris, 150 mM NaCl, 1% Triton X-100, 0.5% sodium deoxycholate, pH 7.5, 2% SDS). The nuclear pellet was solved in 3 mL of S1 (0.25 M Sucrose, 10 mM MgCl2). This solution was layered over 3 mL of S2 (0.35 M Sucrose, 0.5 mM MgCl2), and passed through at 1′430 g for 5 min at 4°C. The nuclear pellet was solved in RIPA buffer as mentioned above. The total protein amount was quantified for all collected fractions by BCA Protein Assay (PierceR, ThermoFisher scientific) according to the manufacturer‘s protocol. 30 μg total protein were taken per sample for each fraction and western blot analysis was performed as mentioned in the immunoblotting section.

HA affinity purification and MS sample preparation

Transgenes encoding HA-miniTurbo tagged ULK1, ATG13, ATG101, FIP200, and HA-MT-GFP (pDS48), as negative ctrl were inducible expressed using 2 mg/mL doxycycline for 24 h in their respective CRISPR KO cells. 2 × 15cm dishes of cells per SILAC label per replicate were used to perform HA-immunoprecipitation using 60 μL slurry of Anti-HA antibody coated magnetic beads (ThermoFisher, 13474229). Cells were lysed in normal lysis buffer; proteins were BCA quantified and equal amount of protein was taken for each label for respective replicates and affinity purification was performed at 4°C on a rotor for 4 h. Further, the beads were washed with lysis buffer and proteins were eluted twice with 30 μL Laemmli buffer at 75°C with 1 mM DTT. The SILAC labels of a replicate were mixed, proteins alkylated with 5.5 mM IAA and fractionated on 4–12% gradient gels. Gel pieces were cut into five fractions, proteins were in-gel digested with trypsin (Promega, V5113). Tryptic peptides were purified by STAGE tips prior to LC-MS/MS measurements. For HA-affinity purification of BAG2 WT and phospho-variants, a similar protocol was performed with few modifications: beads were washed 4 times with lysis buffer after affinity purification, treated with 8 M urea with 1 mM DTT in 50 mM Tris buffer pH 8, transferred onto a 10 kDa MW cut-off filter (Vivacon 500, 10,000 MWCO, Sartorius Cat#VN01H02) and spun at 10′000 g for 30 min. Proteins on the filter were alkylated with 5.5 mM IAA, spun at 10K g for 30 min and washed twice with 50 mM Tris buffer. Protein digestion for MS analysis was performed overnight according to the FASP protocol.[101] Peptides were eluted twice with 200 μL with 50 mM Tris buffer into fresh tubes by centrifugation at 14′000 *g* for 30 min. Eluates were acidified with 5 μL formic acid to a final concentration of ~1% and desalted by STAGE tips prior to LC-MS/MS measurements.

Proximity labeling and streptavidin-based affinity purifications

Expressions of N/C-terminal fusions genes encoding HA-miniTurbo fused to ULK1, ATG13, ATG101 and FIP200 (i.e., gene-of-interest (GOI)), were induced by 2 mg/mL doxycycline, in heavy, medium, light SILAC labeled cells for 24 h. All the GOIs were expressed in their respective CRISPR KO cells. Heavy and medium labeled cells were expressing N-terminal and C-terminal fusion constructs of the above GOIs and for one out of three replicates the labels were swapped. Light labeled cells were always kept as negative control expressing doxycycline-inducible miniTurbo-GFP fusion construct in their respective knockout cells. All these cells were passaged 12 h before induction and 36 h prior to HBSS treatment for 90 min. In parallel, cells were incubated with 400 μM biotin (Sigma Aldrich, B4501) for 90 min along with 10 nM concanamycin A. Cells were washed with 1X PBS on ice for 5 times before harvesting by centrifugation at 3′000 rpm for 2 min and snap freezing in liquid nitrogen before storing the cell pellets at −80°C. For streptavidin-based affinity purification of respective proteins-of-interest (POI), 2 × 15 cm dishes per label and replicate were lysed in RIPA buffer (50 mM Tris, 150 mM NaCl, 1 mM EDTA, 1 mM EGTA, 1% Triton X-100, 0.5% sodium deoxycholate, 0.1% SDS, EDTA-free 1X protease inhibitors (Roche, 11-697-498-001), pH-7.5, 1:5000 Benzonase and 1 mM PMSF). All the above cell lysates were vortexed 4 times for 15 s, and lysis was done for 30 min on ice. Then, lysates were centrifuged at 14′000 rpm for 10 min at 4°C. Protein quantification was determined by BCA assay as per manufacturer's protocol (ThermoFisher, 23225). Equal amounts of proteins were taken in their respective experiments to perform streptavidin (ThermoFischer, Pierce 20361) affinity purification as follows. 100 μL bead slurry was washed 2x with RIPA buffer (without 0.5% sodium deoxycholate, protease inhibitors, PMSF, 0.1% SDS) at RT. Lysates were incubated with beads on a rotor for 90 min. After affinity purification, beads were washed five times with RIPA buffer, three times with TAP lysis buffer (50 mM HEPES-KOH pH 8, 100 mM KCl, 10% glycerol, 2 mM EDTA, 0.1% Triton X-100) and two times with 50 mM ammonium carbonate. Elutions from the beads were performed using Laemmli buffer with 1 mM DTT and 25 mM biotin 75°C for 10 min. SILAC eluates of a respective experiment were mixed to give 150 μL final volume. Protein samples were reduced with 1 mM DTT followed by alkylation with 5.5 μM IAA and ran on 4–12% gradient gels. Gel pieces were sliced to have five fractions per replicate, in-gel digestion with trypsin (Promega) overnight. Peptides were purified via STAGE tips (C18 disc, 3M Empore, Cat#14-386-2) and dissolved in buffer A (0.1% formic acid in MS grade water) prior to LC-MS/MS analysis.

Mass spectrometry-based proteomic analyses

The LC-MS/MS measurements were performed on a QExactive Plus or HF-X mass spectrometer (Thermo Scientific) coupled to an EasyLC 1000 nanoflow-HPLC. Peptides were separated on fused silica HPLC-column tips (I.D. 75 μm, New Objective, self-packed with reprosil-Pur 120 C18-AQ, 1.9 μm [Dr. Maisch] to a length of 20 cm) using a gradient of buffer A (0.1% formic acid in water) and buffer B (0.1% formic acid in 80% acetonitrile in water). Mass spectrometers were operated in the data-dependent mode; after each MS scan (mass range m/z = 370–1750; resolution: 70′000 for QE Plus and 120′000 for HF-X) a maximum of ten, or twelve MS/MS scans were performed using a normalized collision energy of 25%, a target value of 1′000 (QE Plus)/4500 (HF-X) and a resolution of 17′500 for QE Plus and 30′000 for HF-X. MaxQuant software (version 1.6.2.10)[96] was used for analyzing the MS raw files for peak detection, peptide quantification and identification using full length Uniprot human databases (version April 2016/Jan 2022) and common contaminants. Carbamidomethylcysteine was used as fixed modification and N-terminal acetylation, oxidation of methionine, and in case of phosphorylation site analyses phosphorylation of serine, threonine or tyrosine were set as variable modifications. The MS/MS tolerance was set to 20 ppm and four missed cleavages were allowed for Trypsin/P as enzyme specificity. Based on a forward-reverse database, protein and peptide FDR was set to 0.01, minimum peptide length was set to seven, and at least one unique peptide had to be identified. The match-between run option was set to 0.7 min. For whole proteome analyses on the HF-X, the mass spectrometer was operated in the data-independent mode. Briefly, after each survey scan (mass range m/z = 350–1,200; resolution: 120,000) 28 DIA scans with an isolation width of 31.4 m/z were performed covering a total range of precursors from 350-1,200 m/z. AGC target value was set to 3×10^6, resolution to 30,000 and normalized collision energy to 27%. Data were analyzed using Spectronaut software version 15.7 (Biognosys) with standard settings (without imputation) in directDIA mode using reference proteome of Human (UniProt, 2022, full length) and common contaminants. MaxQuant and DIA results were analyzed using Perseus software (version 1.6.2.3).[102]

The MS proteomics data have been deposited to the ProteomeXchange Consortium via the PRIDE partner repository[103]: Project Name: The ULK1 effector BAG2 regulates autophagy initiation by modulating AMBRA1 localization; Project accession: PXD044974. reviewer_pxd044974@ebi.ac.uk.

Halo-LC3 assays

The indicated Halo-rLC3B transgenic cells (HeLa WT cells, BAG2 KO cells and BAG2 KD cells with respective scrambled control) were induced for Halo-rLC3B expression for 24 h in 2 mg/mL doxycycline, pulsed for 20 min with 100 nM TMR ligand (Promega, G8251), washed twice in 1x DPBS, and compared in nutrient-rich and starvation conditions for 3 h at 37°C. Western blot analysis was performed for all samples (see above). Experiments were performed in triplicates and autophagy flux was calculated by taking a ratio of densitometric measurements of Halo-only bands in the presence/absence of TMR ligand in the respective cells.

Yeast two-hybrid (Y2H) interaction analysis

For Y2H interaction assays, plasmids expressing bait proteins, fused to the Gal4 DNA-binding domain (G4BD), and prey proteins, fused to the Gal4 activation domain (G4AD), were co-transformed into reporter strain PJ69-4A (Table S2A).[104] Y2H interactions were documented by spotting representative transformants in 10-fold serial dilution steps onto SC-Leu-Trp (-LT), SC-Leu-Trp-His (-HLT; *HIS3* reporter), and SC-Leu-Trp-Ade (-ALT; *ADE2* reporter) plates, which were incubated for 3 d at 30°C. Growth on SC-Leu-Trp-His plates is indicative of a weak/moderate interaction, whereas only relatively strong interactions permit growth on SC-Leu-Trp-Ade plates. Y2H plasmids were constructed by standard cloning procedures using *Escherichia coli* DH5α for cloning and plasmid propagation. All cloned DNA fragments generated by PCR amplification were verified by sequencing. More information on the plasmids, which are listed in Table S2B, and for yeast strains in Table S2A, are available upon request.

QUANTIFICATION AND STATISTICAL ANALYSIS

MS quantification and statistical analysis

To determine significantly enriched interactors or neighbors of the ULK1 holo-complex by AP-MS or PL-MS, respectively, following criteria were used: a minimum of two valid values per 24 single AP or PL experiments were required. Significantly enriched proteins were determined by outlier tests (Significance A, $p < 0.05$ for AP and $p < 0.05$ BH-corrected for PL-MS, respectively). Proteins had to be significantly enriched in minimal two biological replicates of one specific bait protein.

For the BAG2 interactome analysis, label free quantification measurements were obtained for all samples. All POI APs were bait normalized and the vector control or anti-HA beads control were median normalized. Missing values in control experiments were imputed by normal distributions with a width of 0.3 and a down shift of 1.8. Proteins with FDR corrected $q < 0.05$ values were considered significantly enriched in BAG2 WT and phospho-variants comparing against vector control or anti-HA beads control. These significantly enriched proteins were compared in stimulus-dependent APs (nutrient-rich and starvation conditions): BAG2 WT and phospho-variants BAG2 S31A and BAG2 S31E. Proteins significantly enriched with $q < 0.05$ and $p < 0.05$ were highlighted in respective figures. Perseus software (Version 1.6.2.3) was used for all statistical analysis.

For image-based colocalization analyses the Mander‘s coefficient per cell was determined. In general, 20 cells were analyzed per condition and biological replicated. To address the nested structure of data, i.e., day of the observation and the number cells, significance was determined with a two-way ANOVA using the condition and the replicate as factors following a TukeyHSD post-hoc test to identify significant differences between two conditions.